



Permeability Evolution During Shear Zone Initiation in Low-Porosity Rocks

Christian Kluge^{1,2} · Guido Blöcher¹ · Auke Barnhoorn² · Jean Schmittbuhl³ · David Bruhn^{1,2}

Received: 30 June 2020 / Accepted: 28 December 2020 / Published online: 9 February 2021
© The Author(s) 2021

Abstract

Using an innovative experimental set-up (Punch-Through Shear test), we initiated a shear zone (microfault) in Flechtingen sandstone and Odenwald granite under in situ reservoir conditions while monitoring permeability and fracture dilation evolution. The shear zone, which has a cylindrical geometry, is produced by a self-designed piston assembly that punches down the inner part of the sample. Permeability and fracture dilation were measured for the entire duration of the experiment. After the shear zone generation, the imposed shear displacement was increased to 1.2 mm and pore pressure changes of ± 5 or ± 10 MPa were applied cyclically to simulate injection and production scenarios. Thin sections and image analysis tools were used to identify microstructural features of the shear zone. The geometry of the shear zone is shown to follow a self-affine scaling invariance, similar to the fracture surface roughness. The permeability evolution related to the onset of the fracture zone is different for both rocks: almost no enhancement for the Flechtingen sandstone and an increase of more than 2 orders of magnitude for the Odenwald granite. Further shear displacement resulted in a slight increase in permeability. A fault compaction is observed after shear relaxation which is associated to a permeability decrease by a factor more than 3. Permeability changes during pressure cycling are reversible when varying the effective pressure. The difference in permeability enhancement between the sandstone and the granite is related to the larger width of the shear zones.

Keywords Microfault · Fracture permeability · Microstructure · Fault architecture · Roughness · Sandstone · Granite

1 Introduction

Discontinuities in the upper crust control the hydro-mechanical behaviour of rock masses. They are essential to understand the potentials and limitations of subsurface engineering applications, as well as the structural evolution of geological environments. Laboratory experiments are a substantial element to characterise subsurface discontinuities at a small scale. They are also important for providing reliable data to support the growing number of numerical studies and to describe the complexity of geologic features.

Faulkner et al. (2010) reviewed the advances in studies about fault zones and emphasised that structure, mechanics and fluid flow properties cannot be studied separately. Faults in the field are classically studied from outcrops where the dimensions of faults range from millimetres to decameters, and even kilometre-scale (e.g., Candela et al. 2012; Myers and Aydin 2004). From structural features, qualitative assumptions on hydraulic properties of faults are usually made (e.g., Faulkner et al. 2010; Fossen et al. 2007; Evans et al. 1997; Fisher and Knipe 2001). On the laboratory scale, fault properties at scales ranging from μm to cm, such as microstructural features of fault zones, can be studied. Several studies describe fault initiation and propagation, as well as the fault properties on the microscale (e.g., Chambon et al. 2006; Janssen et al. 2001; Wibberley et al. 2000; Zang et al. 2000; Vermilye and Scholz 1999; Moore and Lockner 1995; Wong 1982).

Tri-axial compression tests are the most common testing procedure to generate a shear zone in a previously intact rock sample. Supplemented with a controlled fluid pressure system, they allow the measurement of the related

✉ Christian Kluge
christian.kluge@gfz-potsdam.de

¹ Helmholtz Centre Potsdam - GFZ German Research Centre for Geosciences, Telegrafenberg, 14473 Potsdam, Germany

² Department of Geoscience and Engineering, Delft University of Technology, PO Box 5048, 2600 GA Delft, The Netherlands

³ Institut de Physique du Globe de Strasbourg, UMR 7516, 5 rue Ren Descartes, 67084 Strasbourg Cedex, France

hydraulic-mechanical properties, such as permeability and dilation (e.g., Chen et al. 2014; Faulkner and Armitage 2013; Mitchell and Faulkner 2008; Teufel 1987). In tri-axial testing, conjugated shear fractures at a certain angle with respect to the loading direction are generated. By its inclination, the conjugated shear fractures are subjected to a displacement in a compressional direction. To apply a normal stress to a shear fracture with a displacement parallel to the shear loading direction, shear box tests were often used but proved difficult to generate a single shear fracture (e.g., Zhang et al. 2019; Elkhoury et al. 2011; Faoro et al. 2009). Direct-shear experiments on core samples with saw-cut fractures or 3D-printed fractures were also used in the past (Ishibashi et al. 2020; Fang et al. 2018; Im et al. 2018; Fang et al. 2017). Such simplified surface geometries allow us to investigate specific physical processes that control, for example, frictional properties or permeability during shearing. However, they cannot depict the variety of structural features commonly found in a natural shear zone (Kluge et al. 2020; Ye and Ghassemi 2019).

The micro-structure of faults has been studied extensively on outcrops and laboratory samples in all types of rocks. In crystalline rocks such as granite, the fracture properties depend on the mineralogy, grain size and mineral strength, as well as the existence of links between microfractures and joints (e.g., Pollard 2005; Hansen and Schmittbuhl 2003; Amitrano and Schmittbuhl 2002; Lockner et al. 1991). Fracture initiation and propagation is assumed to be caused by the coalescence of tensile microfractures formed during loading, oriented parallel to the maximum principal stress (Barnhoorn et al. 2010; Cox and Scholz 1988). The micro-structure of a fault is highly dependent on the amount of deformation or displacement (Cox and Scholz 1988) and involves different deformation mechanisms. This includes mode I and II cracks, inter- or intragranular fractures, cataclastic flow and sub-shear band localisation (Amitrano and Schmittbuhl 2002). For sandstones, a distinction between low- and high-porosity rock is commonly made. This is because porosity and consequently grain size and grain distribution have the largest impact on the structural features forming during shearing (Faulkner et al. 2010; Dunn et al. 1973). But also the phyllosilicate content, lithification and diagenesis are important parameters (Fisher and Knipe 1998).

Permeability differences between deformation bands, the most common feature of faults in porous sandstones, and intact rocks can be up to five orders of magnitude (Fossen et al. 2007). In low-permeability rocks like clay-bearing sandstones, two competitive mechanisms have been described to control the permeability of faults: clay-coating and grain-contact cementation and the existence of fault smear from cataclasis and grain crushing during shear (Fisher and Knipe 2001). These microstructural observations

are actually rarely related to the hydraulic properties during fracture generation. This is why there is need for relating the development of small-scale fault architecture to the evolution of the permeability.

The sustainability of shear fracture permeability is crucial for understanding the long-term performance of fault zones or induced shear fractures in, for example, deep geothermal applications. Commonly, the behaviour of shear fractures is approximated from experimentally displaced tensile fractures in the laboratory. The fracture closure and the related permeability behaviour under varying normal and shear stresses can, thus, be determined (e.g., Hofmann et al. 2016; Milsch et al. 2016; Watanabe et al. 2009; Barton et al. 1985). Typically, an artificial shear displacement is applied to a tensile fracture generated independently. This results in the absence of a damage zone and the asperity deformation related to shear dilation. Therefore, innovative experimental set-ups are needed to generate realistic fault zones and to monitor the evolution of their hydraulic properties.

The Punch-Through Shear (PTS) test was originally developed to obtain the mode II fracture toughness of rocks (Backers and Stephansson 2012). This testing set-up has been adapted to quantify the permeability evolution during fault generation under saturated conditions with a rate or pressure controlled fluid flow (Kluge et al. 2020). In our experiments, we relate the evolution of hydraulic properties, such as permeability, to microstructural observations in shear zones on a laboratory scale (microfault). We will first describe the experimental procedures of the PTS test and present the laboratory results. After that, we will show the procedures and results of the microstructural analysis. Finally, we will discuss the microfault propagation and architecture, their impact on the measured hydraulic properties, as well as their impact on the sustainability of fracture permeability.

2 Materials and Methods

2.1 Testing Equipment

The Punch-Through Shear (PTS) tests were carried out in a conventional MTS tri-axial compression cell. The stiff, servo-controlled loading frame (MTS 815, Material Testing Systems Corporation) holds a loading capacity of up to 4600 kN (load cell calibrated to 1000 kN, calibration error < 1%) and a servo-controlled maximum hydrostatic confining pressure of 140 MPa applied via an oil-filled pressure vessel coupled to an external pressure intensifier. The pore fluid pressure was applied via four Quizix fluid pressure pumps (Model C6000-10K-HC-AT) with a maximum fluid pressure of 70 MPa. Flow-through was continuously applied at a minimum of 2 MPa confining

pressure using two paired upstream pumps and two paired downstream pumps. The differential fluid pressure, which is the difference between in- and outflow pressure, was measured using a differential pressure sensor (Honeywell HL-Z; range: 1 MPa; line pressure max. 35 MPa; precision: $\sim 1\%$). Changes in circumferential strain were measured using a LVDT extensometer chain. All experiments were performed at ambient temperatures of 25–30 °C. Data were recorded at a frequency of 1 Hz. A detailed description of the apparatus can be found in Pei et al. (2016).

2.2 Sample Material

Samples were cored from two different rocks: Odenwald granite and Flechtingen sandstone. All hydro-mechanical parameters of these two types of rocks are listed in Table 1 (data are from Blöcher et al. 2019).

The Odenwald Granite (PGR6-RI) was taken from a quarry near Rimbach in the Upper Rhine Graben, Germany.

It is a Carboniferous, fresh granite showing no sign of alterations or strong micro-fracturing (Fig. 1a, b). It is composed of quartz (Qtz) with a grain size ranging from 1 to 3 mm, feldspar (Fsp) between 2 and 3 mm and mica (Mca) between 1 and 3 mm. The minerals are evenly distributed. Quartz, as well as the darker and brighter mica are the main constituents in our samples, while feldspars are less frequent. Micro-fractures are sparse and cut through grains. They are mostly found within the less compliant quartz, or exist along grain boundaries with no visible shear offset. The porosity is less than 0.6% and the permeability is less than $1 \times 10^{-18} \text{ m}^2$.

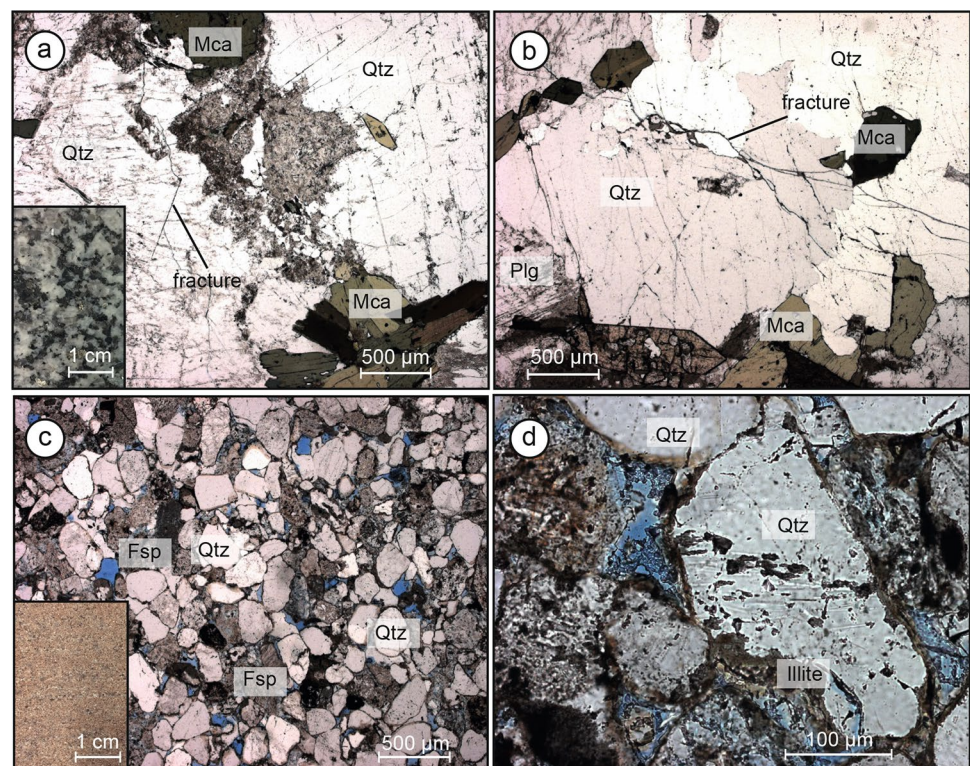
The Flechtingen Sandstone (SBT6-BE) was taken from a quarry near Magdeburg in the North German Basin, Germany. It is a Permian, arkosic litharenite with quartz, feldspars and rock fragments of mainly volcanic origin, about 8% of clay, predominantly illite and chlorite (Fig. 1c, d). This Rotliegend rock is used as an analogue to the sedimentary geothermal reservoirs in the Northern German Basin (Blöcher et al. 2014, 2016). Grain sizes are between 0.05 and 0.2 mm for the feldspar and 0.1–0.5 mm for the

Table 1 Intact rock properties of samples PGR6-RI and SBT6-BE (Blöcher et al. 2019)

| | TS (MPa) | K_{IC} (MPa m ^{0.5}) | UCS (MPa) | E (GPa) | ν (-) | ϕ (%) | k_0 (m ²) |
|---------|------------|----------------------------------|-------------|-----------|-----------|------------|-------------------------|
| PGR6-RI | 11.8 | 1.347 | 131 | 43.8 | 0.22 | < 0.6 | $< 1 \times 10^{-18}$ |
| SBT6-BE | 3.82 | 0.480 | 56 | 14.9 | 0.28 | 8.5 | 2×10^{-16} |

TS tensile strength, K_{IC} mode I fracture toughness, UCS uni-axial compressive strength, E Young's modulus, ν Poisson ratio, ϕ porosity, k_0 initial permeability

Fig. 1 Thin section images of the intact sample material of Odenwald granite (PGR6-RI) and Flechtingen sandstone (SBT6-BE)



quartz, and are partly rounded and well sorted. Contrary to the findings by Hassanzadegan et al. (2014), almost no micro-fractures were found. The low porosity derives from dense packing of grains, as well as illite-clay partially blocking the pore space by coating the quartz grains. In addition, some grain-contact quartz dissolution is present, which additionally reduces permeability. The sandstone is layered, such that all cores were taken perpendicular to the bedding. The porosity of this rock ranges from 6 and 10%, while the permeability for the intact matrix at 2 MPa is given with $2 \times 10^{-16} \text{ m}^2$.

2.3 Sample Geometry and Experimental Set-up

The Punch-Through Shear (PTS) test allows us to induce a cylindrical shear fracture into an intact sample during fluid injection along the fracture direction. The stress concentrates at the notch tips when loading the sample causes a circular shear fracture (microfault) to propagate from the bottom to the top notch. The experimental set-up and

sample geometry are illustrated in Fig. 2a. A full description of the experimental testing procedure can be found in Kluge et al. (2020). Four tests were performed and are listed with their respective dimensions and testing conditions in Table 2.

2.4 Experimental Procedure

The dry samples were jacketed in a heat-shrink tube and installed into the tri-axial compression cell at nearly vacuum conditions of 1 kPa using a vacuum pump (Laboxact SEM 820). Then, they were saturated with distilled water under vacuum conditions and a confining pressure of 2 MPa and a constant pore fluid pressure of 0.2 MPa. Saturation was ended when no more fluid flowed into the sample. This took at least three days for the granite samples and at least 24 h for the sandstone. A constant inflow rate of 0.2–1 ml/min was applied to measure permeability. The fluid was injected from the bottom over the entire cross-sectional area of the sample, A, via an injection grid in the end caps. When the in- and outflow pressure and flow rate was constant, the Darcy

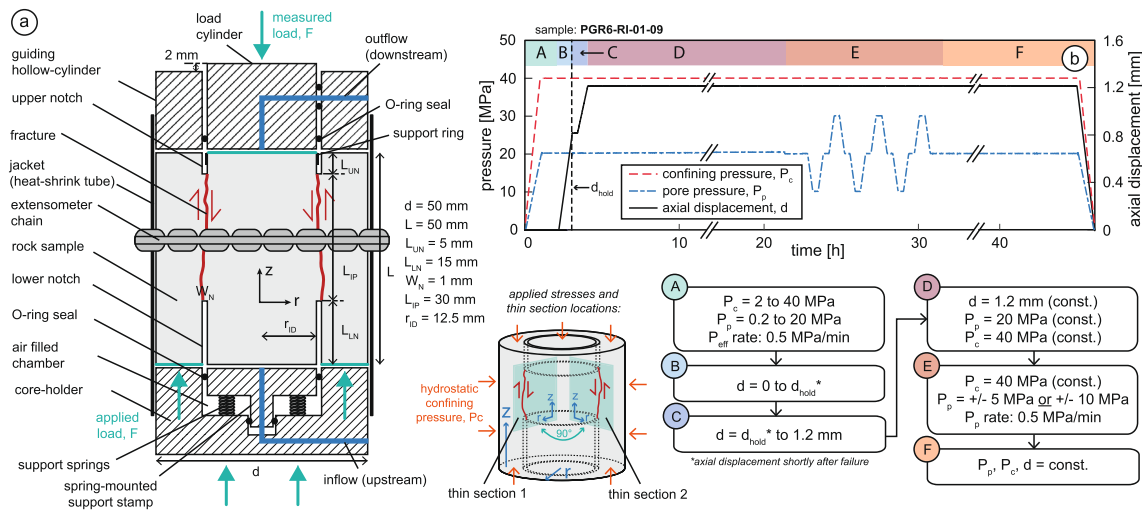


Fig. 2 Experimental set-up and sample dimension of the Punch-Through-Shear test (a) and experimental procedure for all tests (b)

Table 2 List of samples, sample dimensions and testing conditions

| Sample ID | L_{IP} , L , d (mm) | Testing conditions |
|---------------|---------------------------|--|
| PGR6-RI-01-08 | 30.15, 50.15, 50.10 | Faulting: $P_c = 40$ MPa, $P_p = 20$ MPa Pressure cycling: $P_p \pm 5$ MPa |
| PGR6-RI-01-09 | 30.18, 50.18, 50.10 | Faulting: $P_c = 40$ MPa, $P_p = 20$ MPa Pressure cycling: $P_p \pm 10$ MPa |
| SBT6-BE-03-01 | 30.00, 50.00, 50.10 | Faulting: $P_c = 40$ MPa, $P_p = 20$ MPa Pressure cycling: $P_p \pm 5$ MPa |
| SBT6-BE-03-02 | 30.07, 50.07, 50.10 | Faulting: $P_c = 40$ MPa, $P_p = 20$ MPa Pressure cycling: $P_p \pm 10$ MPa |

L_{IP} length of intact portion, L sample length, d sample diameter, P_c confining pressure, P_p pore pressure

permeability was measured. Sample permeability, k , was calculated from Eq. 1 using Darcy's law (Darcy 1856), where the length, L_{IP} , is the distance between the lower and upper notch (Fig. 2a). This distance corresponds to the maximum pressure difference, Δp_f , along the micro-fault (Kluge et al. 2020):

$$k = \frac{Q}{A} \frac{\mu L_{IP}}{\Delta p_f}. \quad (1)$$

Here, Q is the volumetric inflow rate in m^3/s , A is the cross-sectional area of the entire sample in m^2 , μ is the dynamic viscosity of the fluid (Pa s), L_{IP} is the distance between the notches of the sample in meter and Δp_f is the differential fluid pressure in Pa. To verify laminar flow conditions, three different flow rates were applied and the resulting differential fluid pressure was obtained. Flow rate and differential fluid pressure were then checked for linearity at experimental stages of constant stress and displacement. The minimum measurable permeability of our apparatus is around $k = 10^{-18} m^2$. During the entire duration of the experiment, the change in circumference, dU , was measured using the LVDT extensometer chain around the sample. This enables us to calculate the mechanical fracture dilation, e_{mech} , related to the mechanical fracture aperture:

$$e_{mech} = dU/2\pi. \quad (2)$$

It is important to note that the fracture dilation is a measure of the bulk deformation of rock matrix and fracture. Terzaghi's effective pressure, p_e , is defined as the confining pressure, p_c , minus fluid pressure, p_p (Eq. 3) (Terzaghi 1925). The pore fluid pressure was estimated by the outflow pressure, $p_{p,out}$, and the difference in fluid pressures, $p_{p,in} - p_{p,out}$, divided by two (Eq. 4), assuming a linear pressure distribution (Kluge et al. 2020):

$$p_e = p_c - p_p \quad (3)$$

$$p_p = p_{p,out} + \frac{p_{p,in} - p_{p,out}}{2}. \quad (4)$$

The experimental procedure and a flow chart are illustrated in Fig. 2b. Before loading the sample axially to generate the fracture, pore and confining pressures were increased simultaneously to 20 and 40 MPa, respectively, within 1 h. An axial load was then applied by a constant axial displacement at a rate of 0.001 mm/s, pushing the inner loading cylinder down and generating a shear fracture. A drop in the axial load, F , indicated the loss of sample integrity and the consequent existence of a fracture connecting bottom and top notches. The fracturing process is described in detail in Kluge et al. (2020). To allow the pore pressure to reach steady state conditions, the axial displacement was stopped after a clear indication of failure given by the load curve.

During loading and until the hold phase, permeability was assumed to be non-steady state. Assuming that the hydraulic diffusivity of the rock matrix itself, D_r , was constant during the experiments, it was calculated from Eq. 5 using the permeability, k , the Skempton coefficient, B , the drained bulk modulus, K_d , the fluid viscosity, η , and the Biot coefficient, α (Nicolas et al. 2020):

$$D_r = \frac{kBK_d}{\eta\alpha}. \quad (5)$$

This results in a hydraulic matrix diffusivity of 4.5×10^{-6} and $1.1 \times 10^{-4} m^2/s$ for the Odenwald granite and Flechtingen sandstone, respectively. Using the diffusivity values, we calculate the diffusion process over the length of the sample, L , was therefore about 10 min for the Odenwald granite and 0.4 min for the Flechtingen sandstone. We used a time range of about 30 min to reach steady-state flow conditions. After that, the axial displacement was again increased at a slower rate of 0.0001 mm/s leading to an increase in shear displacement until a maximum of around 1.2 mm. Finally, the axial position of the upper loading cylinder was maintained to measure changes in stress. The piston position was constant for at least 14 h, while continuously measuring Darcy permeability and dilation. The cyclic effective pressure changes were applied by varying the outflow pressure by ± 5 or ± 10 MPa at a rate of 0.5 MPa/min. The permeability measurements during the pore pressure cycling were therefore point measurements at the respective stress levels, i.e. after 20–30 min of holding (Fig. 2).

3 Experimental Results

In the following sections, we will present the evolution of the axial load, F , the sample permeability, k , and the mechanical fracture dilation, e_{mech} . Their evolution is shown during fracture generation and shearing (Fig. 3a, c, e), as well as during the constant displacement phase of about 14 h (Fig. 3b, d, f). After that, we show the permeability and fracture dilation evolution during the pore pressure cycling (Fig. 4).

3.1 Fracture Generation

The loading curves of the granite and sandstone samples tested showed a similar behaviour (Fig. 3a). The loading amplitude and the slope in the linear elastic region differ. The curve shows a higher strength and higher elasticity of the granite samples compared to the sandstone. The onset of fracture initiation in the PTS test can usually be determined by the change in inflow and outflow rate, as well as the volume change in combination with the change in slope of the load curve (Kluge et al. 2020). The change in inflow

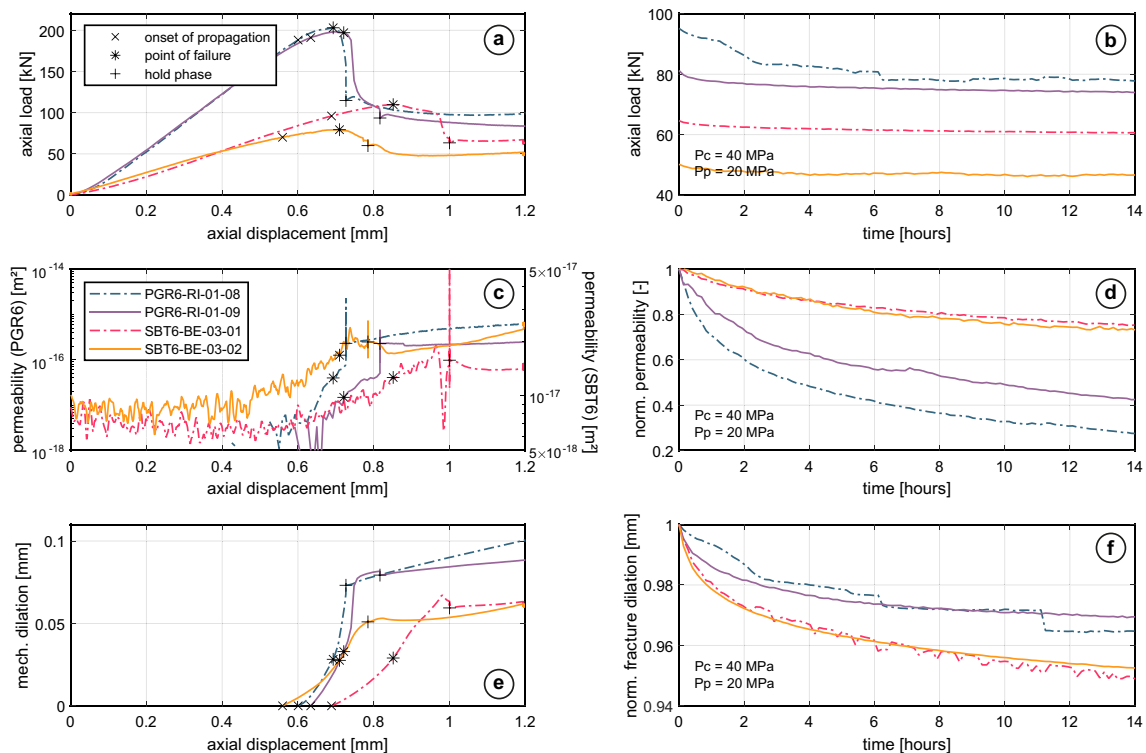


Fig. 3 Axial load (a), the permeability (b) and mechanical fracture dilation (c) evolution vs. axial displacement of the Odenwald granite (PGR6-RI-01-08 and PGR6-RI-01-09) and Flechtingen sandstone samples (SBT6-BE-03-01 and SBT6-BE-03-02) during loading, fail-

ure and shearing. Axial load (d), normalised permeability (e) and mechanical fracture dilation (f) evolution of all samples during the constant displacement phase over 14 h

rate indicated an increase in fracture porosity being flooded. The increase in outflow rate shortly before failure indicated a through-going fracture connecting bottom and top notch.

The apparent permeability, calculated from Eq. 1, of the two granite samples (PGR6-RI-01-08 and 09) started to increase at about 70% of the peak load, i.e. an axial displacement of about 0.6 mm. This corresponded to the change in slope of the load-displacement curve (Fig. 3a). The sample integrity was lost after the load started to decrease indicating the development of a through-going fracture at a displacement of about 0.7 mm. Sample SBT6-BE-03-01 started yielding at about 0.55 mm, with failure at about 0.7 mm, similar to the granite samples. SBT6-BE-03-01 failed at a displacement of 0.85 mm, which was higher compared to all other samples. The peak load was rather plateau-like and the drop in load at about 0.95 mm was also delayed (Fig. 3a).

3.2 Permeability and Fracture Dilation Evolution During Faulting

The point of failure of the granites (PGR6-RI-01-08 and 09) coincided with a sharp increase in fracture dilation calculated from the lateral extensometer data. During fracturing, a continuous increase in dilation was observed even

after peak load (Fig. 3e). During the hold phase, the Darcy permeability was first measured at steady state conditions. The increase in permeability was more than 2 orders of magnitude, from below 1×10^{-18} to about 2.3×10^{-16} m² for both samples (Fig. 3c). The mechanical fracture dilation reached a value of 0.07 and 0.08 mm (Table 3). During shearing, the permeability of sample PGR6-RI-01-08 increased from 2.3×10^{-16} to 6.0×10^{-16} m², while the permeability of sample PGR6-RI-01-09 remained relatively constant at around 2.3×10^{-16} m². A similar trend as for permeability was observed for the fracture dilation. Here, sample PGR6-RI-01-08 showed an increase from 0.07 to 0.1 mm, while sample PGR6-RI-01-09 showed an increase from 0.08 mm to almost 0.09 mm.

The pre-failure permeability of both sandstone samples (SBT6-BE-03-01 and 02) was about 1×10^{-17} m². The permeability of both samples decreased during the linear elastic loading phase (Fig. 3c). At about 0.6 mm, similar to the granite, the permeability started to increase. Sample SBT6-BE-03-01 showed a delayed increase. The permeability increased to 1.6×10^{-17} and 2.0×10^{-17} m² for sample SBT6-BE-03-01 and 02, respectively. The mechanical fracture dilation reached a value of 0.05 and 0.06 mm, which was lower compared to the granite (Fig. 3e). During

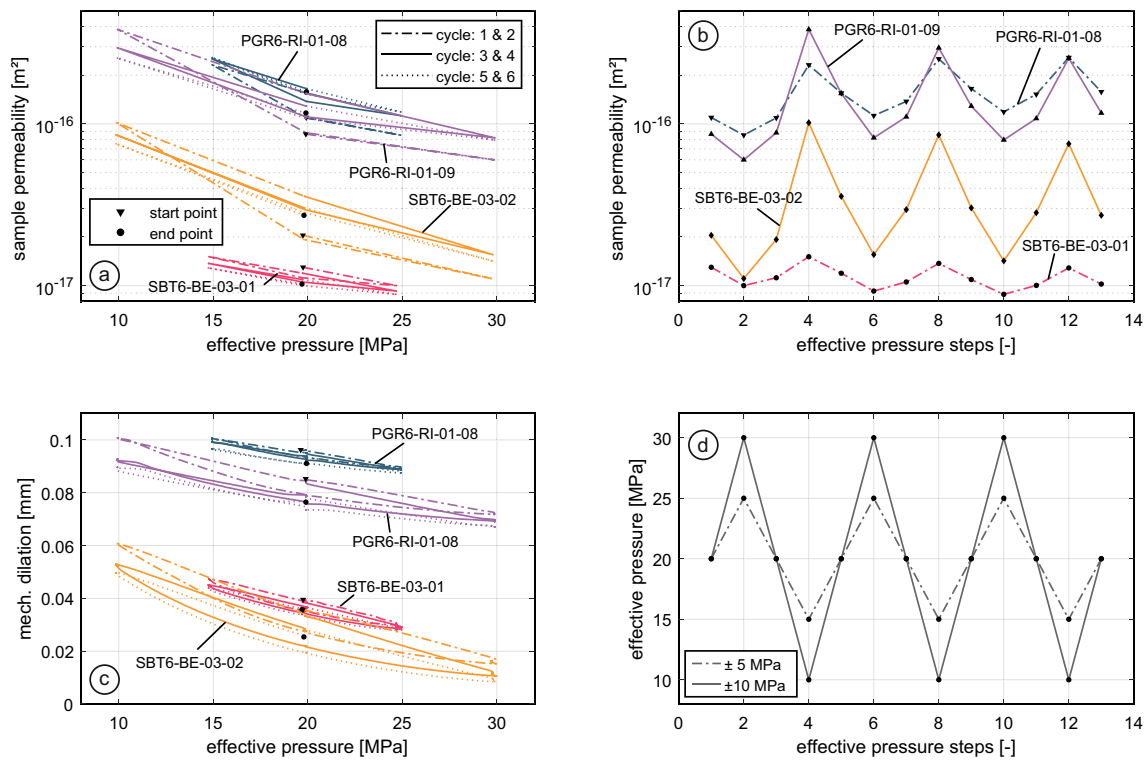


Fig. 4 Permeability and mechanical fracture dilation evolution vs. the effective pressure (a, b) and vs. the effective pressure steps (c, d)

Table 3 Summary of permeability evolution during the respective experimental stages

| Sample ID | k_f/k_0 | k_s/k_f | k_c/k_s | k_p/k_c | k_p/k_0^a |
|---------------|-----------|-----------|-----------|-----------|-------------|
| PGR6-RI-01-08 | 231.1 | 2.8 | 0.3 | 1.4 | 158.0 |
| PGR6-RI-01-09 | 229.5 | 1.0 | 0.4 | 1.4 | 116.8 |
| SBT6-BE-03-01 | 1.8 | 0.8 | 0.7 | 0.8 | 1.2 |
| SBT6-BE-03-02 | 2.0 | 1.2 | 0.7 | 1.3 | 2.7 |

k_0 intact sample permeability, k_f after faulting, k_s after shearing, k_c after compaction, k_p after cyclic pressure loading

^aTotal enhancement before and after the experiment

further shearing the permeability remained constant for both samples at about 1.5×10^{-17} and 2.0×10^{-17} m². Fracture dilation during shearing again followed the same trend as for the permeability: it remained relatively constant for sample SBT6-BE-03-01 at around 0.06 mm. A slight increase from 0.05 to 0.06 mm was measured for sample SBT6-BE-03-02.

After that, the axial displacement was stopped and kept constant until the end of the experiment. Permeability was measured over the time span of at least 14 h to monitor possible longer term changes in stress, permeability and dilation (Fig. 3b, d, f). The reduction of the measured axial load after fracture generation and shearing was largest in

the first 2 h. The axial load then reached an almost stable value and was overall higher for the granites (Fig. 3b). Figure 3d shows, that the permeability of the granites was reduced by a factor of about 3.3 and 2.5. Permeability of the two sandstone samples was reduced by a factor of about 1.4. Still, the dilation of the sandstone was larger compared to the granite (Fig. 3f).

The results of the permeability changes during the respective experimental stages are summarised in Table 3.

3.3 Permeability Evolution During Pore Pressure Cycling

The change in permeability and fracture dilation during effective pressure changes is crucial for an understanding of the sustainability of fractured reservoirs. Therefore, the pore pressure was varied at a constant confining pressure by ± 5 and ± 10 MPa for one sandstone and one granite sample, respectively (Fig. 4). The permeability in Fig. 4a, b is given as a point measurement at the respective effective pressure level.

During the pore pressure changes of ± 5 MPa, the permeability magnitude was in the range of 8.5×10^{-17} to 2.5×10^{-16} m² for the Odenwald granite and between 8.8×10^{-18} and 1.5×10^{-17} m² for the Flechtingen sandstone. Permeability changes of the granite and sandstone

were rather reversible. A slight permanent reduction in permeability for the sandstone and a slight increase for the granite after six loading cycles was found (Table 3). The fracture dilation showed a similar reversible behaviour, although the fracture dilation of the sandstone was half compared to the dilation of the granite (Fig. 4c). The mean dilation calculated from the lateral extensometer data represents the bulk changes in circumference caused by matrix and fracture.

During pore pressure changes of ± 10 MPa, the permeability magnitude was in the range of 6.0×10^{-17} and 3.8×10^{-16} m², for the Odenwald granite and between 1.1×10^{-17} to 1.0×10^{-16} m² for the Flechtingen sandstone. These range of reversible changes in permeability were overall larger compared to the ± 5 MPa pressure changes. Interestingly, the permeability after six pressure cycles was slightly increased for the granite and the sandstone compared to before the pressure changes (Table 3). The change in mean fracture dilation was larger compared to pressure changes of ± 5 MPa, with a slight permanent reduction after six pressure changes (Fig. 4c). The total range of dilation was larger for the sandstone compared to the granite. This implicates a higher deformability of the sandstone matrix and fracture system.

Considering the slopes of the permeability changes (Fig. 4b), the magnitude of the effective pressure dependent permeability change depends on the previous stress level (Fig. 4d). When the effective pressure reduced from 25 or 30 MPa to 20 MPa, permeability changes were larger compared to unloading from 20 MPa to 15 or 10 MPa. Loading the sample from lower effective pressure (10 or 15 MPa to 20 MPa) led to larger changes in permeability compared to loading from 20 MPa to 25 or 30 MPa. Permeability changes of the Odenwald granite were always larger compared to changes of the Flechtingen sandstone.

4 Microstructural Analysis of Microfault Geometry

Two thin sections were cut from each sample, both vertically in the r and z -direction (cylindrical coordinates, see Fig. 2a). They depict the entire microfault between both notches (~ 30 mm). Blue epoxy was injected into the sample before preparing the thin sections to visualise the void spaces and microfractures. The fault zone geometry was analysed with and without polarised light to identify the fault zone dimensions and geometrical features. Image analysis was performed to quantify the fault properties (Table 4).

4.1 Fault Geometry in the Odenwald Granite (PGR6-RI)

Two thin sections from each sample were prepared along the z -direction to show the full extent of the fault between the two notches. The inferred direction of maximum principal stress, the flow direction, as well the orientation of the thin section images within the sample are shown in Fig. 5a, b.

A fault core, i.e. a zone where the two fracture faces were clearly separated and displaced, and a surrounding damage zone is visible in all samples. The fractures in the damage zone are oriented mainly 20° – 30° to the displacement direction. They are, therefore, not typical Riedel structures (10° – 20°) and occurred mainly as intragranular fractures. The absence of shear displacement led us assume that they are tensile mode fractures with apertures in the μm range. Some small fractures connected the tensile fractures in the damage zone.

Other fractures grew radially in the r -direction and are stress-relaxation fractures formed during unloading in tensile mode (Kluge et al. 2020). Damage zone fractures are highly present in quartz and plagioclase grains, but rather localised or absent in mica grains. Fault particles are brecciated, mostly elongated and very different in size. In plagioclase, identified by their striations, a similar brecciated fault core can be observed with a maximum width of about 2 mm (Fig. 6a). K-feldspar minerals, without striations, are locally weathered and produced very fine-grained and thin fault gouge (Fig. 6b). Micas were deformed in three different modes: brittle, plastic or smeared out (Fig. 6c, d). Although some mica grains were clearly displaced, they were partly deformed without showing any clear microfractures or void spaces. The plastic deformation of micas resulted in a discontinuous fault core, i.e. no visible void space, at some locations (Fig. 5).

Larger tensile fractures in mainly stiff minerals formed transensional wedges that lack features of brittle deformation (Fig. 6e). These wedges can be understood as step-over structures connecting zones of simple shear. In weaker minerals, such as mica or feldspar, the fault is

Table 4 Properties of fault architecture from the image analysis of the thin sections

| Thin section ID | $n_{f,t}$ (-) | $\bar{w}_{dz,e}$ [σ] (mm) | \bar{w}_{fc} [σ] (mm) | H_{sd} (-) | H_{ld} (-) |
|-----------------|------------------|------------------------------------|----------------------------------|-----------------|-----------------|
| PGR6-RI-08-01-2 | 0.07 | 0.63 [0.35] | 0.41 [0.19] | 0.65 | 0.28 |
| PGR6-RI-09-01-2 | 0.07 | 0.93 [0.42] | 0.60 [0.51] | 0.63 | 0.31 |
| SBT6-BE-03-01-1 | 0.04 | 0.99 [0.46] | 0.19 [0.13] | 0.63 | 0.16 |
| SBT6-BE-03-01-2 | 0.04 | 0.82 [0.45] | 0.27 [0.15] | 0.65 | 0.16 |

$n_{frac,t}$ fracture density threshold, \bar{w}_{dz} mean damage zone width, \bar{w}_{fc} mean fault core width, H_{sd} Hurst exponent for small distances, H_{ld} Hurst exponent for large distances, σ standard deviation

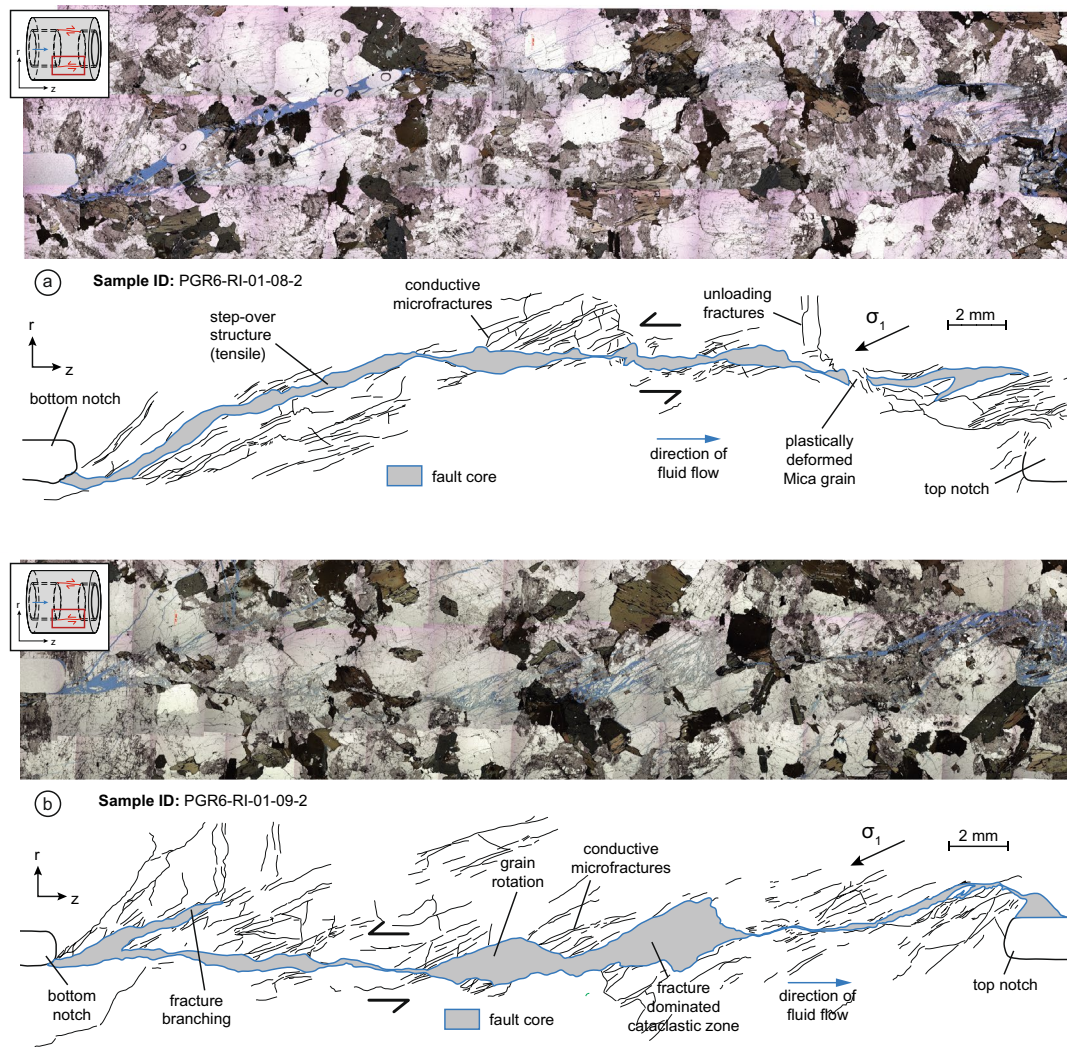


Fig. 5 Overview of the microfault connecting the lower and upper notch of the sample in thin section and interpretative drawings below indicating the structural features of a granite sample PGR6-RI-01-08-2 (a) and PGR6-RI-01-09-2 (b)

characterised by simple shear. In simple shear, faulting is parallel to the displacement direction, which produced a very fine fault gouge (Fig. 6f). In some areas, the orientation changed into compressional or transpressional regimes. Here, the fault core is very thin and shows several splay fractures (Fig. 6f).

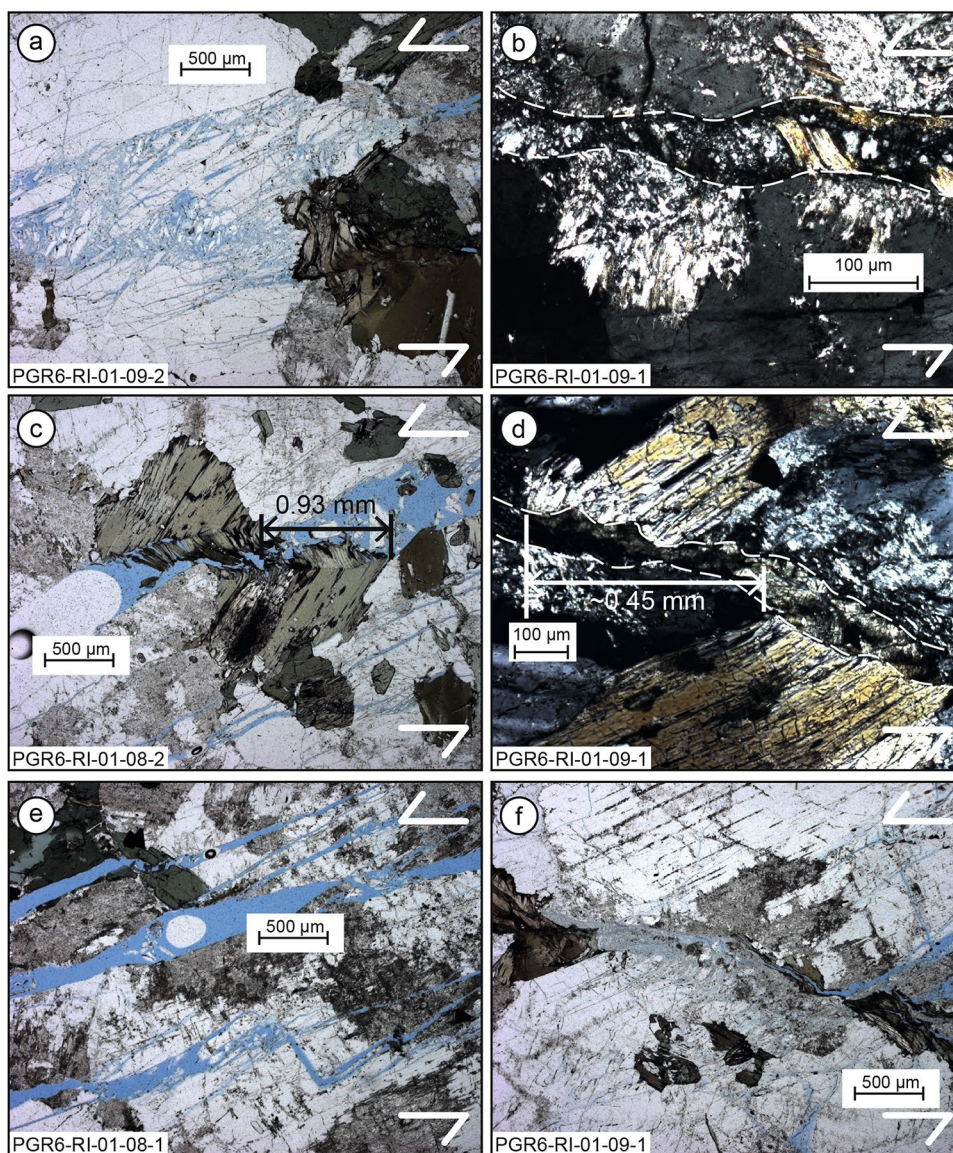
The formation of joints, wedges and cavities enabled additional slip accommodation (Segall and Pollard 1983). The relative displacement was measured at displaced mica minerals at certain locations and varied from 0.45 to 0.93 mm (Fig. 6c, d). This is less than the applied axial displacement of 1.2 mm. The fracture branches were hydraulically isolated from the main fault zone, as we could not detect any microfractures connecting them to the main fault.

4.2 Fault Geometry in the Flechtingen Sandstone (SBT6-BE)

Two thin sections from the sandstone samples were taken along the z -direction. They showed a narrower, but also continuous fault zone connecting the upper and lower notches of the sample. The inferred direction of maximum principal stress, the flow direction, as well the orientation of the thin section images within the sample are shown for an overview in Fig. 7a, b.

In areas where the fault core was straight, it showed a rather constant width (Fig. 8a). The fractures in the damage zone were either intragranular or intergranular and were, thus, isolated from each other, since clay was found in

Fig. 6 Detailed view of cataclastic rock fragments in quartz (a), fine fault gouge filling the fault core (b), displaced mica minerals (c, d), tensional fractures (e) and fault core compression (f) in the Odenwald granite thin sections



between the grains (Fig. 1c, d). Furthermore, intragranular fractures were mainly extensional fractures sub-parallel to the maximum compressive stress direction. The clay that originally coated the quartz minerals was smeared across the fault core and produced a very fine gouge (Fig. 8b). The fault mostly propagated along grain boundaries (intergranular). Only in some locations, the quartz grains were brecciated and partially rotated (Fig. 8c, d).

In areas of transpression and simple shear, the fault zone was extremely narrow with clay smear and other fine particles along the fault zone (Fig. 8c, d). The fault was wider and more open for fluids when the fault core was oriented similar to the damage zone fractures, i.e. 20° – 30° to the axial displacement direction (Fig. 8e). Splay fractures, typical for large scale faults (Myers and Aydin 2004), were found to develop in areas of fault compression

(Fig. 8f). Step-over structures were absent in the sandstone samples, contrary to the granite fault. Furthermore, most of the displacement was accommodated by the fault core or shear band itself. Rarely any deformation or displacement accommodation was found in the damage zone. Strain accommodation within the surrounding rock matrix was hard to identify from our images.

4.3 Image Analysis and Shear Zone Width

To compute the width of the shear zone perpendicular to the flow direction (in z -direction) from the thin section images, we used a combined approach using the software tools IMAGEJ (Schneider et al. 2012) and MATLAB (see Appendix for detailed description). The width, w , was defined as the open area of a profile perpendicular to the fracture

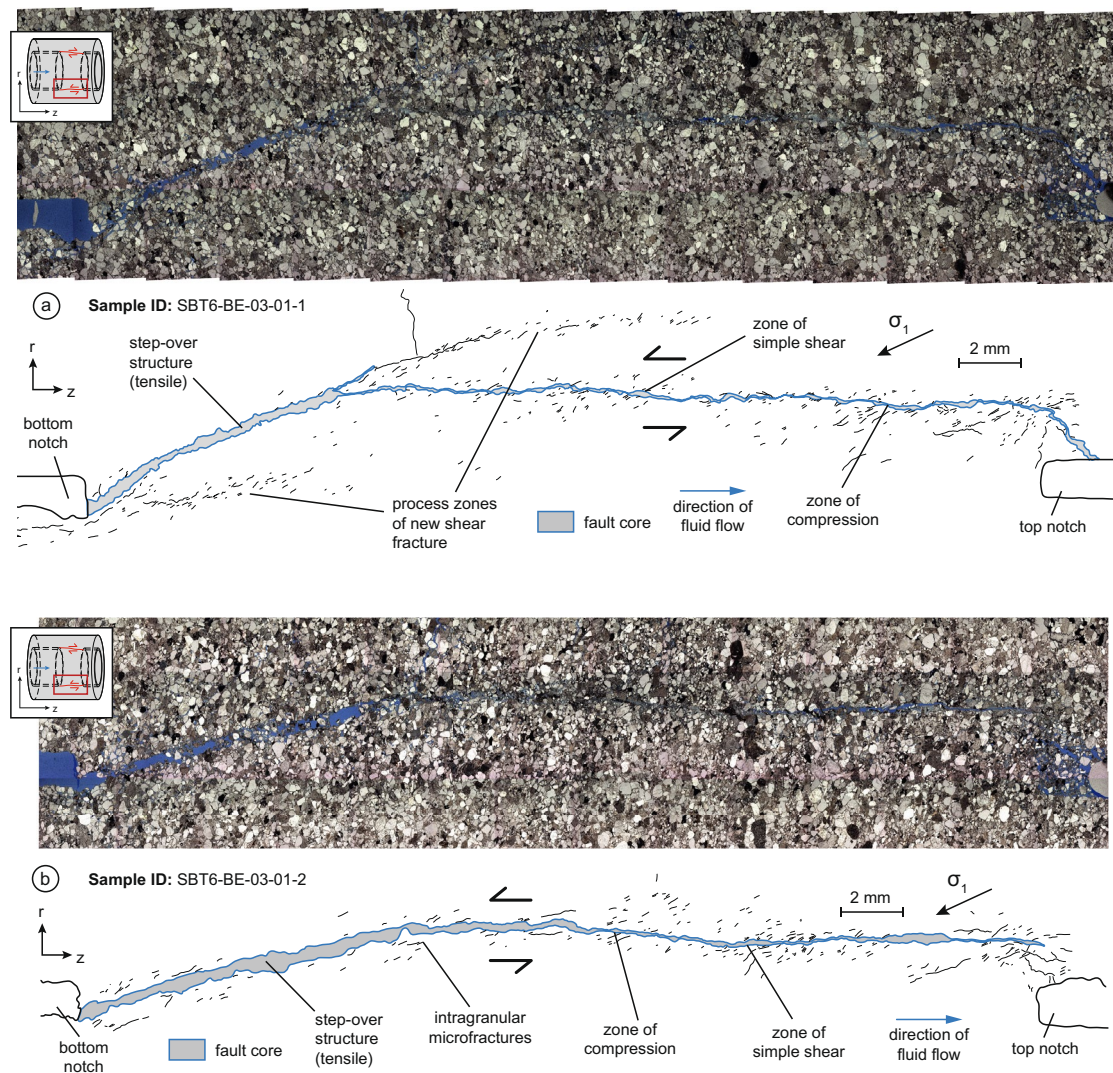
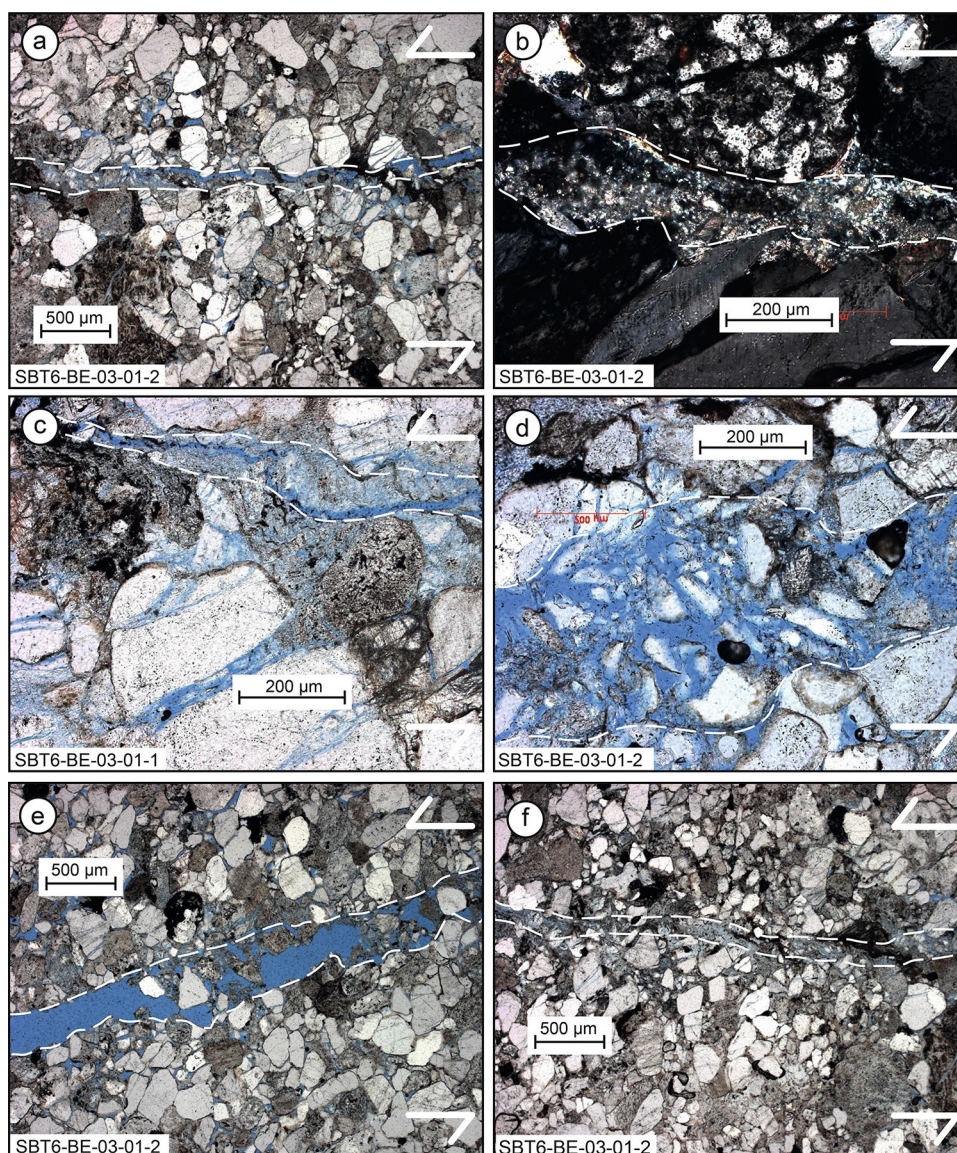


Fig. 7 Overview of the microfault connecting the lower and upper notch of the sample in thin section and interpretative drawings below indicating the structural features of a sandstone sample SBT6-BE-03-01-1 (a) and SBT6-BE-03-01-2 (b)

and corresponds to the measured mechanical fracture dilation, e_{mech} , i.e. the opening of the fault perpendicular to the flow. First, the blue epoxy in the thin section images was extracted by separating the respective Hue Saturation Brightness (HSB) colour range from the remaining colours present. We assume that the epoxy filled the entire void space. The extracted binary image of the pore space was then imported to Matlab. A sliding square filter was applied to calculate the fracture density, n_f , defined as the numbers of black pixels (void space) divided by the number of total pixels inside one window (144). We used a window size of 12 by 12 pixels, corresponding to $3.5 \mu\text{m}$ by $3.5 \mu\text{m}$. This resulted in a fracture density distribution of the fault zone and the surrounding damage zone (Fig. 9a, b). To obtain a fracture density distribution along the fracture, we used two

different approaches: (1) we shifted the maximum fracture density towards the center in the direction perpendicular to flow or (2) we sorted the fracture densities in ascending order to then calculate the distribution with the maximum in the center (see Appendix). Shifting the fracture density led to a distribution where the damage zone (low fracture density) was visible to the left and right of the normal distribution. The sorted distribution was smoother with the noise included in the normal distribution. To separate the actual shear zone from the surrounding rock matrix, we used a threshold for the minimum fracture density to be considered as part of the shear zone. As fracture density threshold value, $n_{f,t}$, we used the intersection point of the shifted and sorted distribution assuming that at this point the fractures in the damage zone (noise) become dominant (see Appendix). This

Fig. 8 Detailed view of the narrow fault core (a), fine fault gouge filling the fault core (b), grain splitting (c), grain fragmentation (d), tensional fractures (e) and fault core compression (f) in the Flechtingen sandstone thin sections



value must be higher than the background noise, which was the mean fracture density in the damage zone surrounding the fault core.

We then calculated the shear zone width by summing up all windows with a fracture density higher than the fracture density threshold, $n_{f,t}$:

$$w = l_{px} \sum_1^{N_{px}} n_f |_{n_f > n_{f,t}}, \quad (6)$$

where w is the width, l_{px} is the length of a pixel (3.5 μm), N_{px} is the number of pixels of a profile, n_f is the fracture density in a single window reduced to a single pixel and $n_{f,t}$ is the fracture density threshold. The fracture density distribution for the granite and sandstone with their shear zone thicknesses are shown in Fig. 9c. The fracture density

already shows, that this calculation included high fracture densities outside the main fracture, especially for the sandstone sample. This possibly led to an overestimation of the fault zone width. Therefore, we considered this width as the effective damage zone width, $w_{dz,e}$. The mean damage zone width, $\bar{w}_{dz,e}$, was defined as the mean of the damage zone width of all profiles along the z -direction. The calculated values were 0.93 mm (± 0.42 mm) for the granite and 0.99 mm (± 0.46 mm) for the sandstone (Table 4). This width was similar for both rocks in the transtensional areas close to the lower notch. In the simple shear and transpressional regimes, however, the sandstone fault was thinner.

In a second approach, we extracted the fault core based on our structural interpretation of the thin sections (Figs. 5 and 7). We then applied the same procedure as for the original image (Fig. 9a, b). Computing the width of the extracted

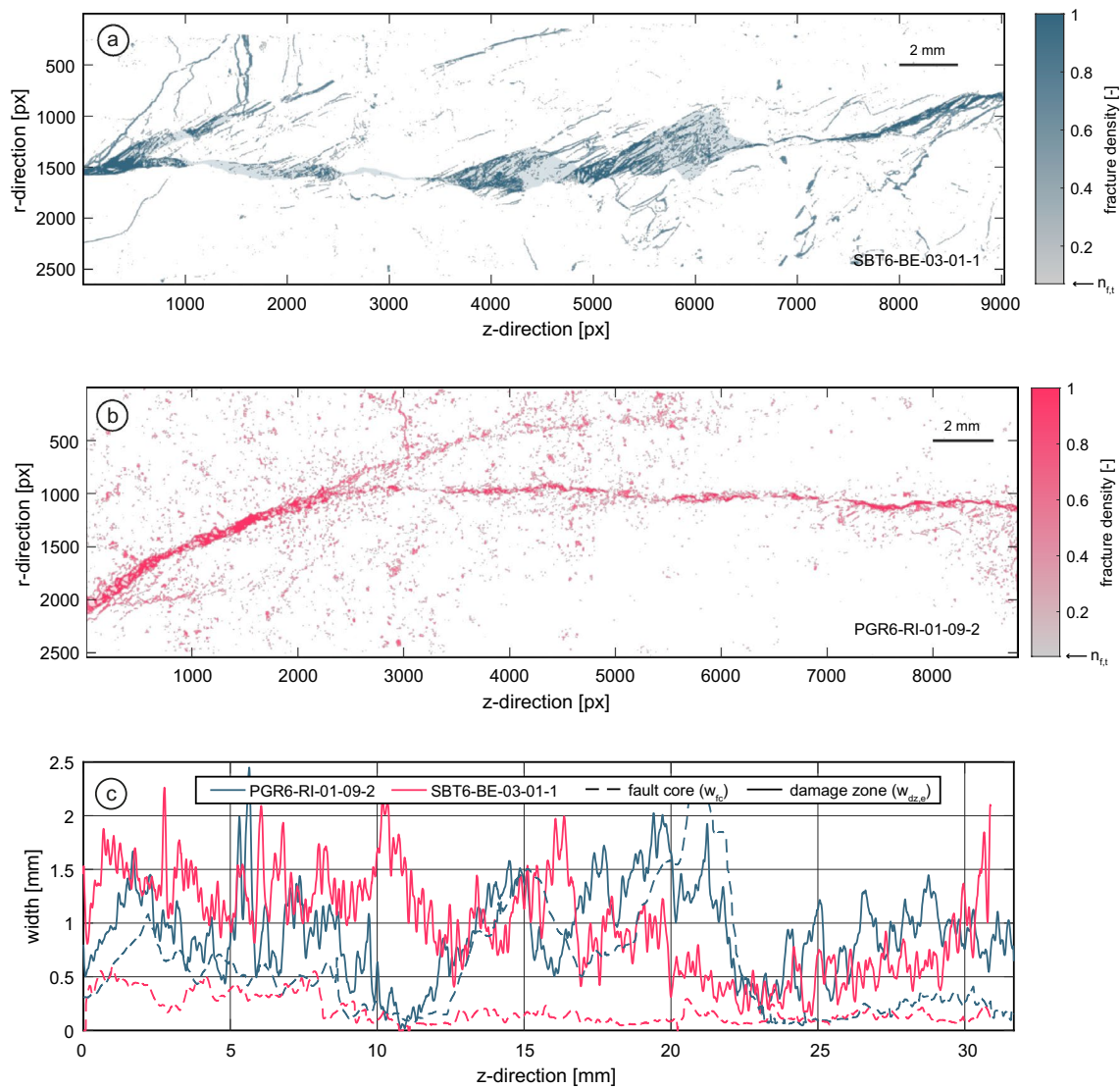


Fig. 9 Fracture density of the original image (blue or red) and the extracted fault core (grey) in the Odenwald granite (PGR6-RI-01-09-2) (a) and Flechtingen sandstone (SBT6-BE-03-01-1) (b). The effective damage zone width, $w_{dz,e}$, and fault core width, w_{fc} , of both rocks (c)

fault core with the same threshold, $n_{f,t}$, we found that the fault core width, w_{fc} , was much smaller for the extracted fault core in the sandstone samples compared the effective damage zone width, $w_{dz,e}$ (Fig. 9c). The fracture density threshold, $n_{f,t}$, must be about 0.5, to obtain a similar value of the mean effective damage zone width, $w_{dz,e}$, compared to the mean fault core thickness, \bar{w}_{fc} . For the sandstone, \bar{w}_{fc} was about 0.2 mm. The mean fault core width of granite was 0.60 mm (± 0.51 mm) and 0.19 mm (± 0.13 mm) for the sandstone (Table 4). In the granite sample, the thickness of the extracted fault core was little reduced compared to that of the original image.

We assume that analyzing the original image by extracting the entire void space of the image, we obtained the effective damage zone width, $w_{dz,e}$, or the cumulative area of flow.

The analysis of the extracted fault core allows us to calculate its width, w_{fc} , based on the structural deformation. Comparing the width of the sandstone and granite samples (Table 4), we see a narrower fault core for the sandstone sample.

4.4 Variations in Shear Zone Width

Additionally, we calculated the spatial correlations of the width fluctuations along the fracture (in z-direction) using a self-affine geometrical model with a roughness exponent, H (Candela et al. 2009, 2012; Schmittbuhl et al. 1995). Here, we assume that the 2D profile width follows (Meakin 1998):

$$\delta x \rightarrow \lambda \delta x, \quad \delta z \rightarrow \lambda^H \delta z, \quad (7)$$

where δx is the coordinate along the 2D profile and δz the amplitude. Therefore, we calculated the power spectrum and the semi-variogram of the width fluctuations (Schmittbuhl et al. 1995). The width profiles have a resolution of 3.5 μm in the z -direction and were linearly detrended (Schmittbuhl et al. 1995). The data comprised 9000 data points for each profile. Due to the logarithmic scale of the variogram and power spectrum, the data density of the frequencies and lag distances vary. To consider equal weights of each data point for the fitting procedure, we re-sampled the data points with equidistance in log-space representing the raw data. As a result, we generated 100 data points as a mean from the raw data for further analysis. The Hurst exponent of the variogram, H_{var} was calculated from the slope of the variance, σ^2 in mm^2 vs. the lag distance, h in mm:

$$\sigma^2 = h^{2H_{\text{var}}}, \quad (8)$$

where σ^2 is the variance and h the lag distance. The Hurst exponent of the power spectrum, H_{ps} , was calculated from the slope of the frequency spectrum of the fracture width profile in log space using the single-sided spectrum using (Candela et al. 2012):

$$P(k) = Ck^{-1-2H_{\text{ps}}}, \quad (9)$$

where $P(k)$ is the Fourier power spectrum, k is the wave number and C is a pre-factor.

The ranges for the fits were equal for the variogram (lag distance in mm) and the power-spectrum (wave number equals the inverse of the lag distance in 1/mm), for all samples. The results of the roughness calculations are shown in Fig. 10. We found a two power-law behaviour for both the granite and the sandstone samples with a cross-over at about 0.06 mm. The slopes were different for smaller distances between 0.01 and 0.06 mm and larger distances between 0.06 and 3 mm. The roughness exponent for small distances, H_{sd} , was 0.6 and was similar for the granite and sandstone samples. For larger distances the roughness exponent, H_{ld} , was about 0.3 for the granite and 0.15 for the sandstone. A significantly lower roughness exponent at large scales showed that there are lower spatial correlations at large scale than at small scales. The close to zero value for the sandstone is an indication that width fluctuations are uncorrelated random fluctuations. For the granite, the width fluctuations were more spatially correlated at large scales. This evidences strong similarities of the scaling properties of the shear band width for both materials. However, there was a significant difference for roughness exponent at the large scale, suggesting a difference in the width distribution between both rock types. Variogram and power spectrum gave similar results validating the self-affine measurement. Using various fracture density thresholds, $n_{\text{f,t}}$, to calculate the roughness of the

width profiles, we obtained similar roughness exponents up to a deviation of ± 0.1 . Only for the power spectrum at smaller distances, H_{ps} reached a value of above 0.9 for a threshold, $n_{\text{f,t}}$, of 0.5, while the H_{ps} approached zero at larger scales for the sandstone (Fig. 11). The summarised data are given in Table 4, where the mean Hurst exponent from the variogram and power spectrum for each sample and the respective ranges are given.

5 Discussion

5.1 Microfault Propagation and Microfault Architecture

The aim of this paper is to relate macroscopically determined hydraulic and mechanical data to microstructural observations. Therefore, we first discuss the fault propagation mechanisms and structural features. We assume that our observations are related to the sample scale only and that the stress field is not known along the fracture. However, the damage zone microfractures provide a general trend for the largest principal stress (σ_1).

We applied a modified PTS test to generate a shear fracture from an initially intact rock sample with a general orientation parallel to the loading direction (Kluge et al. 2020; Backers and Stephansson 2012). With this test, permeability changes in shear fractures were easy to obtain while shear fracture orientation in space can change with respect to the displacement direction (z -direction). Commonly, shear fractures are generated using tri-axial compression tests. In such tests, intact rock samples are loaded with a differential stress until failure, resulting in an inclined shear fracture at an angle to the loading direction (e.g., Kluge et al. 2017; Mitchell and Faulkner 2008). This complicates any permeability measurement, because the fluid must flow through the matrix before reaching the fracture.

The fault zones in the sandstone and granite were found to change their orientation along the fracture plane leading to transpressional, simple shear and transtensional structures. Our structural observations include mode I and mode II fractures similar to Amitrano and Schmittbuhl (2002) in tri-axial experiments. We found microfractures oriented mainly 20°–30° to the direction of the applied stress in both rock types. These open tensile fractures indicate the maximum principle stress direction (σ_1).

The mineral stiffness is important for the development of the microfractures in the damage zone. In the granite, compliant minerals seem to inhibit microfault-growth, which promotes microcracking in adjacent stiff grains (Wibberley et al. 2000). This seems to enlarge the fault zones compared to the sandstone. Microfractures in

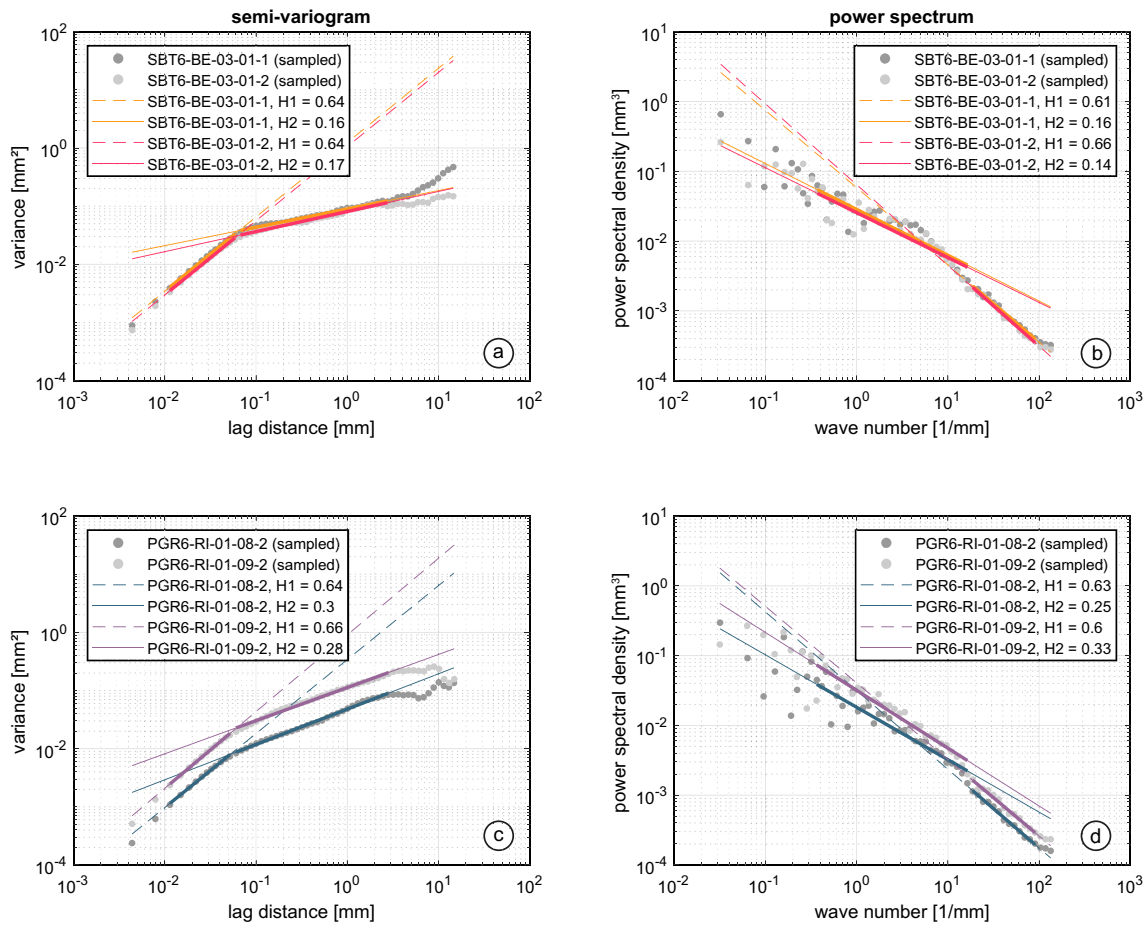


Fig. 10 Semi-variogram (a, b) and power spectrum (c, d) of the width profiles of the Flechtingen sandstone and Odenwald granite resulting from image analysis of the thin sections

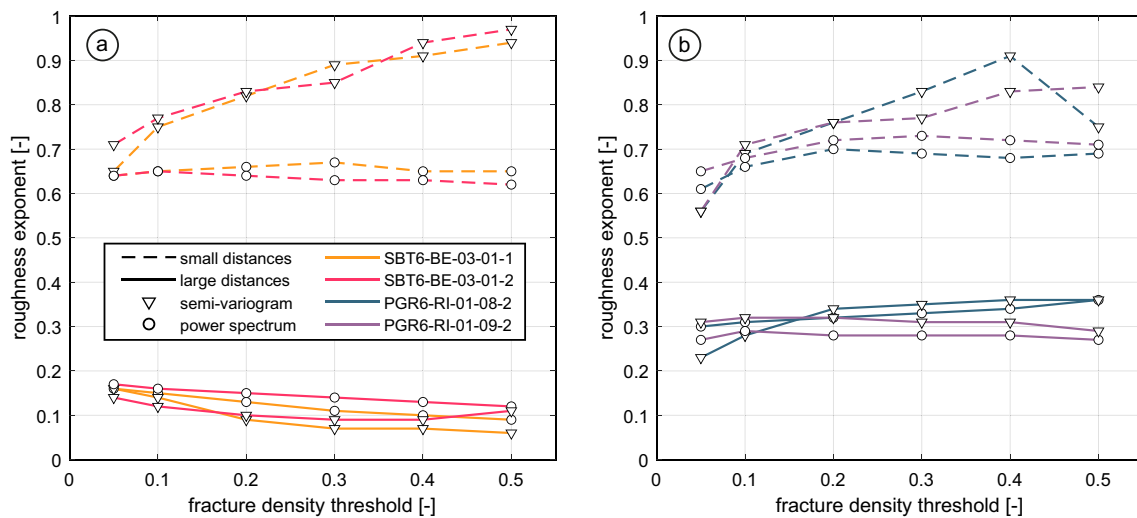


Fig. 11 Roughness exponent, H , for different fracture density thresholds, $n_{f,t}$ for the Flechtingen sandstone (a) and Odenwald granite (b) at the respective small and large distances

granite were partly intergranular while they were, both, intra- and partly inter-granular in the clastic sandstone. This is similar to reports by Cox and Scholz (1988). Stiff minerals, such as quartz or plagioclase fail mainly by tensile splitting of the entire mineral (Figs. 7 and 8). Tensile splitting, previously defined as an echelon splitting (Wibberley et al. 2000), accommodates most of the displacement without generating cataclasis. More compliant minerals, such as mica, behave differently. They deform by either brittle failure, leading to a formation of broken fragments, or by plastic deformation, without fracturing (Fig. 8). This is caused by their anisotropy, such that their orientation within the stress field seems to impact the deformation process.

In low-porosity sandstone rocks, we suggest that the bonding strength between the grains controls the onset of macroscopic fracture propagation, especially in the presence of clay coating. Our experiments showed, that a narrow microfault favours to propagate along grain boundaries (intergranular) rather cutting through mineral grains. Therefore, frictional sliding at the grain boundaries might be a more dominant process than a sudden rupture. This highlights the importance of soft clays. Additionally, no noticeable decrease or increase in damage zone porosity was found. This indicates, that the classification by Fossen et al. (2007) has limitations for smaller scale and low-displacement fault zones.

From the fault zones generated by the PTS test we can describe three stages of fracture generation for both rocks (Fig. 12): microfracture formation (stage I), principal shear-plane formation (stage II) and shearing (stage III).

During loading and after the samples start yielding, the previously described micro-fractures start to form (stage I, Fig. 12a). Yielding was observed at about 70% of the peak load, which is slightly above the previously reported critical dilatancy stress of 50% (Faulkner and Armitage 2013; Vermilye and Scholz 1999). The microfractures are assumed to form prior to the principal shear plane, since they surround the fault core (Dunn et al. 1973). In the sandstone, they reveal the location and orientation of the fracture process zones.

During failure (stage II, Fig. 12b), a macroscopic fracture is assumed to connect these microfractures to form a principal shear plane (Tenthorey and Cox 2006; Vermilye and Scholz 1999; Cox and Scholz 1988). Fracturing starts from the bottom notch of the sample due to the higher shear stress at this point (Kluge et al. 2020; Backers and Stephansson 2012). The notch represents a pre-existing fracture where shear fractures commonly nucleate (Janssen et al. 2001; Reches and Lockner 1994; Segall and Pollard 1983).

With increasing shear displacement (stage III, Fig. 12c) different structures start to develop. Transensional wedges

are present in areas where the principle shear plane is oriented according to the micro-fractures (20° – 30°). Simple shear structures form in areas where the principal shear plane is parallel to the direction of loading. Transpressional zones form where the principal shear plane is oriented normal to the microfractures. These various structures are important for the fluid flow in shear zones, as we show in the next section. During progressive shearing, we did not observe a stress built up and release (stick-slip). We assume that the applied displacement of maximum 1.2 mm leaves the fault in an early stage of fault propagation.

5.2 Impact of Fault Architecture on Hydraulic Properties

The permeability change caused by introducing a microfault into an intact rock sample under in situ pressure conditions gave different results for granite and low-porosity sandstone. The granite showed an increase in permeability of 2–3 orders of magnitude, while the sandstone showed almost no increase in permeability. In the following, we discuss the experimental results with respect to microstructural features separately for Odenwald granite (PGR6-RI) and the Flechtingen sandstone (SBT6-BE).

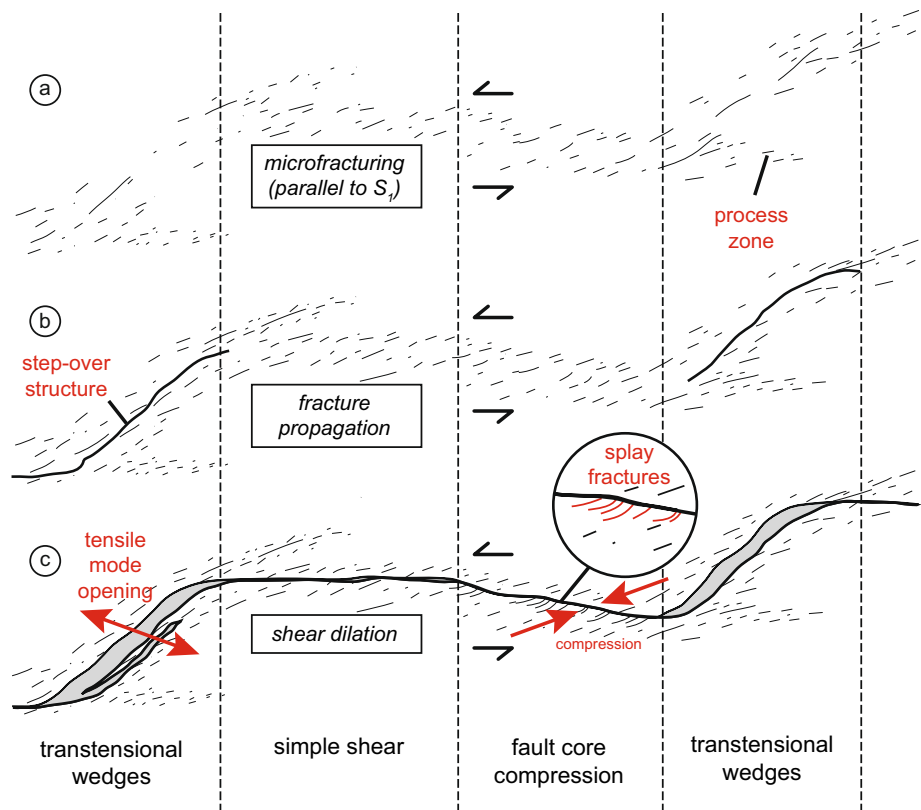
For the granite, we assume the permeability increase is mainly related to the presence of the microfault connecting the lower and upper notches. This is because of the large permeability enhancement measured during microfault generation. The complex microfault architecture, consisting of a damage zone and fault core, mainly controls the fluid flow in the fractured sample.

When the fault zone is comprised of stiff minerals, fracturing due to brittle deformation and grain rotation is promoted. Consequently, in areas with a large quartz content the permeability is likely to be higher compared to areas with less quartz. Micas are critical to the fault permeability since they partially block the fracture porosity. This can be compensated by the existence of a damage zone surrounding impermeable zones. Here, opening mode fractures in the damage zone parallel or sub-parallel to maximum principal stress aid fluid flow.

Grain rotation is limited due to the relatively low applied displacement of 1.2 mm. The strength of the minerals, therefore, controls the frictional properties of the fault. At higher displacements, the grain size of the cataclastic material controls the frictional strength and the hydraulic properties (Stüinitz et al. 2010; Bos and Spiers 2001).

Very little permeability increase was measured during faulting and shearing for the Flechtingen sandstone samples, suggesting that the matrix permeability is higher than the fracture permeability. Fossen et al. (2007) argued that dilatant fractures are common for low-porosity sandstone and compaction bands for high-porosity sandstones. We could

Fig. 12 Interpretational model for the fracture propagation during shear fracture growth with **a** micro-fracturing, **b** fracture propagation and **c** shear dilation, as well as the resulting structural elements of the fault zone



not prove such phenomena. We assume, that the pore-throat fillings and possible grain coating minerals also control permeability since the fault propagates along grain-boundaries. But although the fault might be dilatant in a low-porosity rock, permeability is not necessarily enhanced, especially in the presence of clay. Still, the microstructure indicates that there are open sections (areas of transtension), enhancing fluid flow in flow directions perpendicular to the displacement direction.

We, therefore, suggest to classify the potential fault permeability including the presence of clay, similar to Fisher and Knipe (1998). They distinguished between clean and impure sandstones depending on the presence of more or less than 15% of clay. We already see an impact for the Flechtingen sandstone with 8% of clay. This especially affects low-displacement microfaults, where the damage zone is not fully developed.

Granites potentially have a larger fracture width compared to sandstones, which is an additional explanation for the lower permeability measured in the sandstone samples. The measured fracture dilation, e_{mech} , was about 5–10 times lower for all samples compared to the fault core width, w_{fc} . This possibly resulted from the fact that the fracture re-opened during unloading before preparing the thin sections. Additionally, the fault core width, w_{fc} , ignores particles within the fault core leading to an overestimation of

fracture width. Still, it provides an understanding of the relative width distribution along the fracture. Furthermore, the fracture dilation, e_{mech} , was measured at a single point, at which the measured dilation can be higher or lower than the mean value along the fault (Marache et al. 2008). Lastly, the fracture zone width, w , and the fracture dilation, e_{mech} , were measured perpendicular to the flow direction. But because fractures were often inclined by 20°–30° in areas of transtension, there is an additional aperture error of 6–14%.

We suggest that a self-affine scaling relationship ($\delta x \rightarrow \lambda \delta x$, $\delta z \rightarrow \lambda^H \delta z$) exists not only for the fracture surface roughness (e.g., Candela et al. 2009), but also for the variations in fracture width in shear fractures. We found a two scale regime for roughness, similar to the analysis by Santucci et al. (2010). They related the crossover length scale to fluctuations in fracture toughness and the stress intensity factor, which gave $H = 0.6$ – 0.7 for small scales and $H = 0.3$ for large scales. However, at larger scales, the sandstone gives a lower roughness exponent of about 0.15 compared to the granite with 0.3. This is similar to reports by Boffa et al. (1998). For the sandstone, the scaling relationship is lost at large scales using the power spectrum method, since H approaches zero. This indicates a constant rms-value independent of the scale, such that there is no spatial correlation.

The morphology of the fault controls the dilation potential and therefore the hydraulic properties. The scale-dependent dilation potential from our results can only be described qualitatively. The Odenwald granite showed a more pronounced morphology and a larger variety in structural features. This led to a larger fault zone width and possibly larger permeability compared to the Flechtingen sandstone. The sandstone has lower width fluctuations, a narrower fault core width, w_{fc} , shows clay in the pore-throats and has intergranular fractures in the damage zone. This reduces a potential permeability enhancement. But the much larger effective damage zone width, w_{dze} , and matrix porosity favour fluid flow and deformation around the fracture.

In general, dilational jogs, step-over structures and transensional wedges are favourable for fluid flow. They lead to larger apertures and almost no cataclasis or grain crushing (Janssen et al. 2001). This results in heterogeneous flow directions and increased local pore pressure build-ups when fluid tries to flow from high-aperture zones to low-aperture zones (b). However, the impact of the magnitude of the external stress on fault permeability and structure still needs to be investigated, since several authors already suggested a dependence of fault permeability with confining stress (Wibberley et al. 2000; Zoback and Byerlee 1975).

5.3 Sustainability of Fault Permeability

In the following section, we discuss the fault permeability during variations in effective stress, or in other words, what controls the fracture closure and, therefore, the longevity of the generated permeability.

The largest permeability reduction in both rocks was caused by time-dependent processes after fault generation. Three possible mechanisms need to be considered responsible for fracture closure: (a) chemical rock–fluid interactions, i.e. dissolution or precipitation of minerals (Orywall et al. 2017), (b) fines migration leading to a blockage of fluid pathways within the fault (Blöcher et al. 2016), and (c) mechanical creep, i.e. compaction or rearrangement of fault gouge particles (Hofmann et al. 2016). Mechanical back-slip is not possible, since the axial displacement piston was held in place when monitoring time-dependent permeability changes.

Rock–fluid interactions, re-crystallisation or cementations are not influencing permeability in our short-term experiments. Such processes evolve over long time-scales of several weeks (Yasuhara and Elsworth 2008; Fisher and Knipe 2001) and require saline solution as pore fluid, while we used distilled water.

No fines migration or particle re-distribution was found in the microfaults we analysed. Fine particles or breccia in the fault core were not found to have migrated. Still, finer particles might have been removed by the preparation process when blue epoxy was injected into the sample.

We assume that mechanical closure or power law compaction of the faults was the most contributing effect causing the permeability reduction. This is often reported from laboratory experiments (Im et al. 2018; Hofmann et al. 2016). The permeability decrease of the granite samples follows a power law compaction, possibly by rearrangements of fault gouge material or asperities (Kluge et al. 2020). The permeability loss might be recovered by new slip events (Im et al. 2018), but this was not tested in our experiments. We attribute the permeability loss over time of the sandstone samples to compaction of the matrix and fracture, because of the larger dilation magnitudes, the higher porosity and the smaller fault core.

The reported reversible changes in permeability during effective pressure changes in both rocks are in contrast to existing studies. Other researchers found that any increase in effective pressure leads to a reduction in permeability with an increasing number of stress cycles (e.g., Hofmann et al. 2016; Watanabe et al. 2009; Chen et al. 2000; Pyrak-Nolte and Morris 2000). The amount of permanent permeability changes might be controlled by: (a) the amount of plastic energy in the system, (b) the contact material of the fracture surfaces (c) the effective pressure coefficient.

We suggest that the lower amount of plastic energy in existing fault zones reduced the risk of a permanent fracture closure during changes in effective pressure. The amount of plastic energy depends on the conditions during fracture generation. Fracturing can occur during loading under in situ pressure or at ambient conditions. A high amount of plastic energy is to be expected when fractures are produced at ambient conditions, for example using manually displaced tensile or saw-cut fractures (Fang et al. 2017; Hofmann et al. 2016; Watanabe et al. 2009), as well as artificial fracture surfaces (Ishibashi et al. 2020; Im et al. 2018). Those experiments are representative for artificially generated fractures for example by hydraulic stimulation. Such fractures are potentially critical to larger magnitudes of permanent fracture closure. Our experimental results obtained by the PTS test are more representative for pre-existing shear fractures, possibly generated by tectonic movements. Since they are produced at in situ stress conditions, they are less critical to permanent permeability changes.

We assume that cataclastic fault gouge and plastically deformed mica grains partly control the elastic and

reversible behaviour of permeability. This assumption is supported by the lack of any irreversible deformation, such as fractures oriented perpendicular to the displacement direction or grain crushing. Consequently, the contact points in areas of transpression or simple shearing should be used for modelling crustal strength, similar to what Bos and Spiers (2001) and Niemeijer and Spiers (2005) proposed.

Even larger changes in pore pressure in faults generated by tectonic movements are not necessarily critical to permeability. This is important for faulted low-porosity clastic geothermal reservoirs (Blöcher et al. 2016), as well as natural fault zones in granitic rocks (Genter et al. 2012). But more such evidence is needed on the field scale.

6 Conclusions

We measured the evolution of permeability and fracture dilation using an innovative experimental set-up, the Punch-Through Shear (PTS) test. We observed the following permeability evolution for Odenwald granite and Flechtingen sandstone: (I) fault generation and shearing leads to a permeability enhancement of more than 2 orders of magnitude in Odenwald granite, but an unchanged permeability in low-porosity Flechtingen sandstones. This might be caused by the presence of a larger fault core and a conductive damage zone in the Odenwald granite. The larger matrix permeability, a smaller fault core and the presence of clay lead to no noticeable increase for the low-porosity Flechtingen sandstone. Still, the presence of a variety of structural features might support a heterogeneous flow field independent of the rock type. (II) The highest permeability loss was found during time-dependent processes during the first hours after fracture generation. This is likely caused by compaction of the fracture and re-arrangements of fault particles, as well as the matrix compaction in the Flechtingen sandstone. (III) Pore pressure changes in a fault produced under in situ pressure conditions cause an elastic permeability change. This is due to the low plastic energy contained in the fault zone because of the in situ fracture generation. Therefore, we assume that naturally faulted geothermal reservoirs might have a sufficient hydraulic sustainability considering only mechanical effects.

Thin section observations and image analysis revealed local width changes depending on the structural geometry of the fault: transtension, simple-shear or transpression. In transtensional regimes the permeability might even be increased in sandstone rocks. This would also lead to a

bi-directional permeability, although this cannot be proven by the bulk permeability measurements. Furthermore, the width profiles indicated a self-affine scaling relationship similar to what is commonly observed for fracture surface roughness.

Appendix: Description of the Image Analysis Procedures

To describe the procedure to calculate the width of the fault zone, $w_{dz,e}$ and w_{fc} , we describe the methodology for one thin section images of the granite (PGR6-RI-01-09-2) and sandstone (SBT6-BE-03-01-1), respectively. The fracture density is given by the amount of pixels identified as void space in a window of a certain size. Therefore, a squared sliding filter was applied to the binary image resulting from the extraction of the blue epoxy (HSB range) from the thin section images (Figs. 13a and 14a). The fracture densities were re-arranged by either shifting or sorting the values for each profile along the fault (z -direction). Shifting was performed by finding the maximum fracture density in each profile and shifting the entire profile accordingly using the *circshift* function in MATLAB (Figs. 13b and 14b). Sorting was performed by sorting the fracture density of each profile in ascending order (Figs. 13c and 14c). Both approaches result in a fracture density distribution of each profile (r -direction). These distributions were then stacked along the z -direction, such that the mean distribution could be calculated. This distribution is largely dependent on the window size used for the squared sliding filter. The window size was decided by the largest peak in density distribution for the shifted fracture density. Therefore, several window sizes from 2 by 2 to 92 by 92 pixels were considered. Figure 15a, b shows the fracture density distribution for the shifted fracture density for the granite and sandstone. For too small window sizes, the distribution is smeared out across each stacked profile without a clear peak. Too high window sizes lead to a large smoothing effect showing no clear peak. At a window size of 12 by 12 pixels, we find a clear peak and an even distribution of fracture density across the profiles. Therefore we decided to use a window size of 12 by 12 for our calculations.

Three possible criteria for defining the fracture density threshold value, $n_{f,t}$, were considered: (1) the background noise, (2) the intersection of the sorted and shifted fracture density distribution and (3) sample porosity. For the first criterion we assumed that background noise can be derived from the mean fracture density in an area outside the fault core. Therefore, we have applied the squared sliding filter in

there areas of the sandstone and granite (Figs. 13a and 14a), assuming that this area is less affected by fracturing and calculated the mean fracture density. This analysis resulted in a mean fracture density of 0.003 for the background noise of the granite and 0.015 for the sandstone (Fig. 15c, d). These values, however, were too low when considering this for the shifted fracture density of the entire image, since it is well below the limbs of the distribution. This results in an over-estimation of the fracture width. A second approach was to consider the intersection of the shifted and sorted fracture

density distribution. The intersection of both distributions shows the onset at which the background noise or the fracture density of the damage zone becomes dominant in the shifted distribution. For the granite we found the intersection point of the sorted and shifted distribution width at a fracture density of 0.07 and for the sandstone at 0.04 (Fig. 15e, f). Lastly, the sample porosity was considered as a threshold value, because the porosity of the sample should reflect the porosity in each profile, assuming that all porosity is filled with blue epoxy. However, the porosity for the granite is less

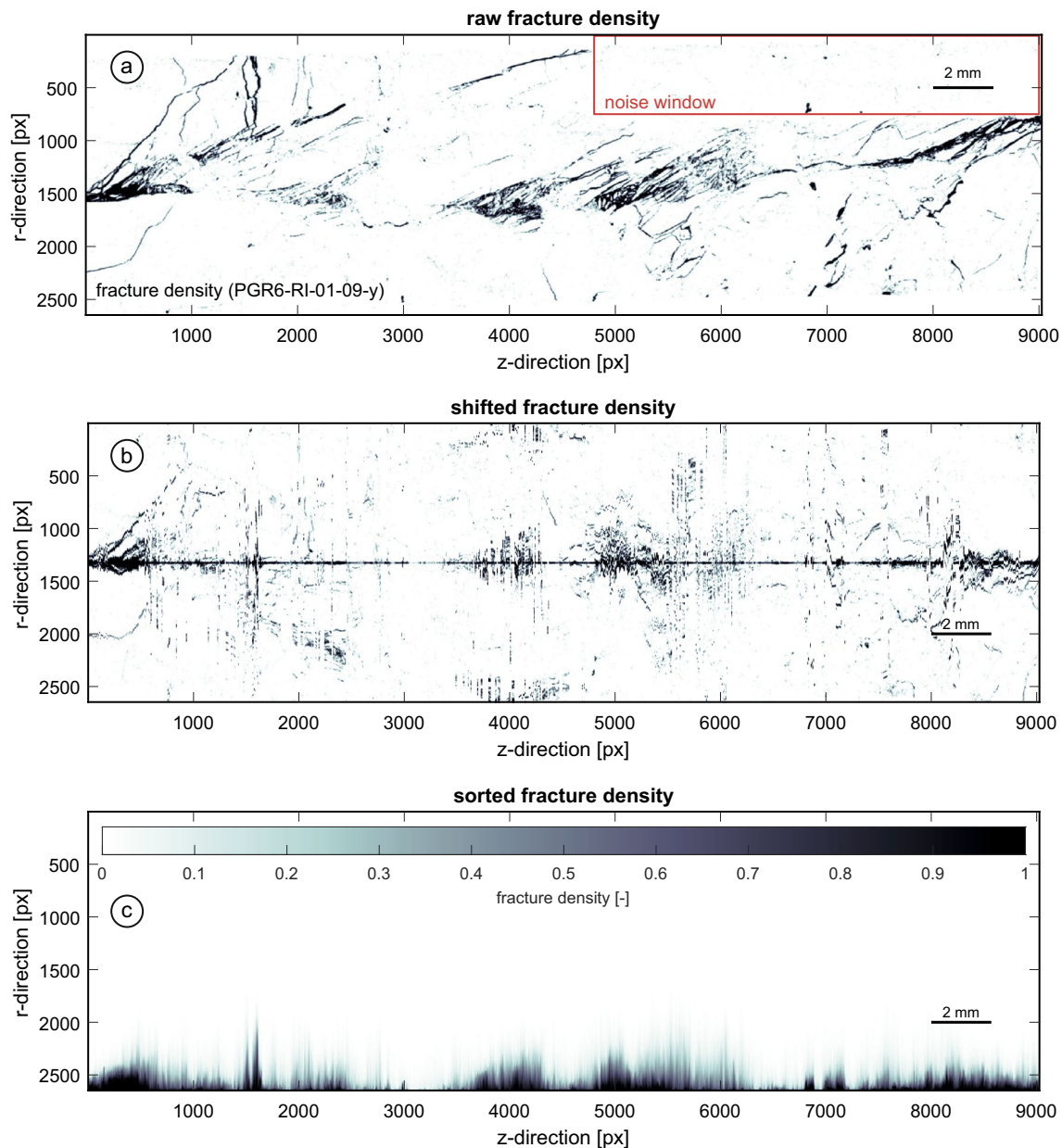


Fig. 13 Fracture density of the original binary image (a), as well as the shifted (b) and sorted (c) fracture density of granite sample PGR6-RI-01-09-2

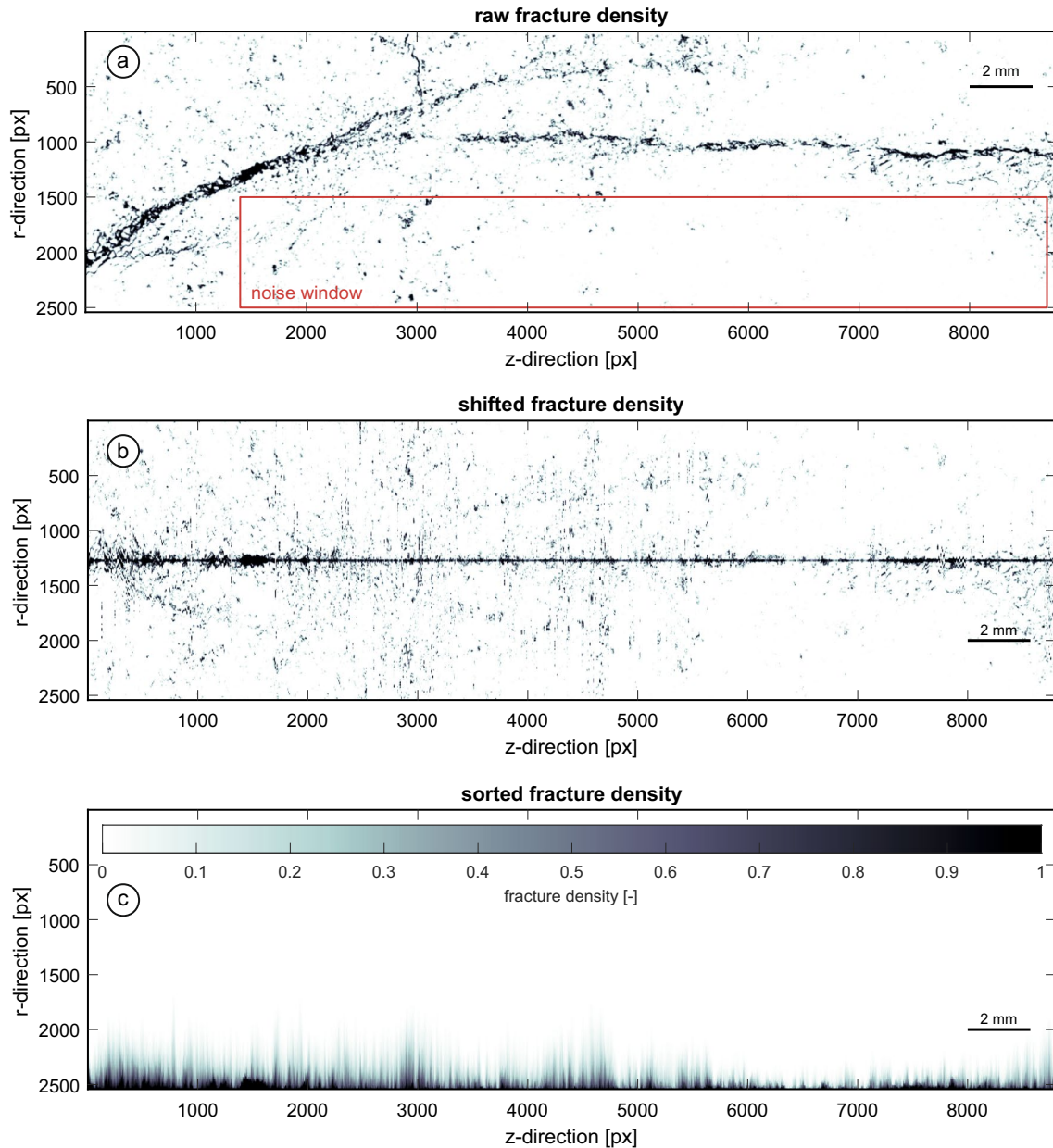


Fig. 14 Fracture density of the original binary image (a), as well as the shifted (b) and sorted (c) fracture density of sandstone sample SBT6-BE-03-01-1

than 1% resulting in a fracture density threshold of 0.01, which is below the measured noise. In contrast, the porosity of the sandstone is about 7.5% resulting in a fracture density threshold of 0.07, which is larger than the intersection

point of the shifted and sorted distribution. Comparing all three methods and the resulting shear zone width (Fig. 12), we decided for the intersection point method to define the fracture density threshold.

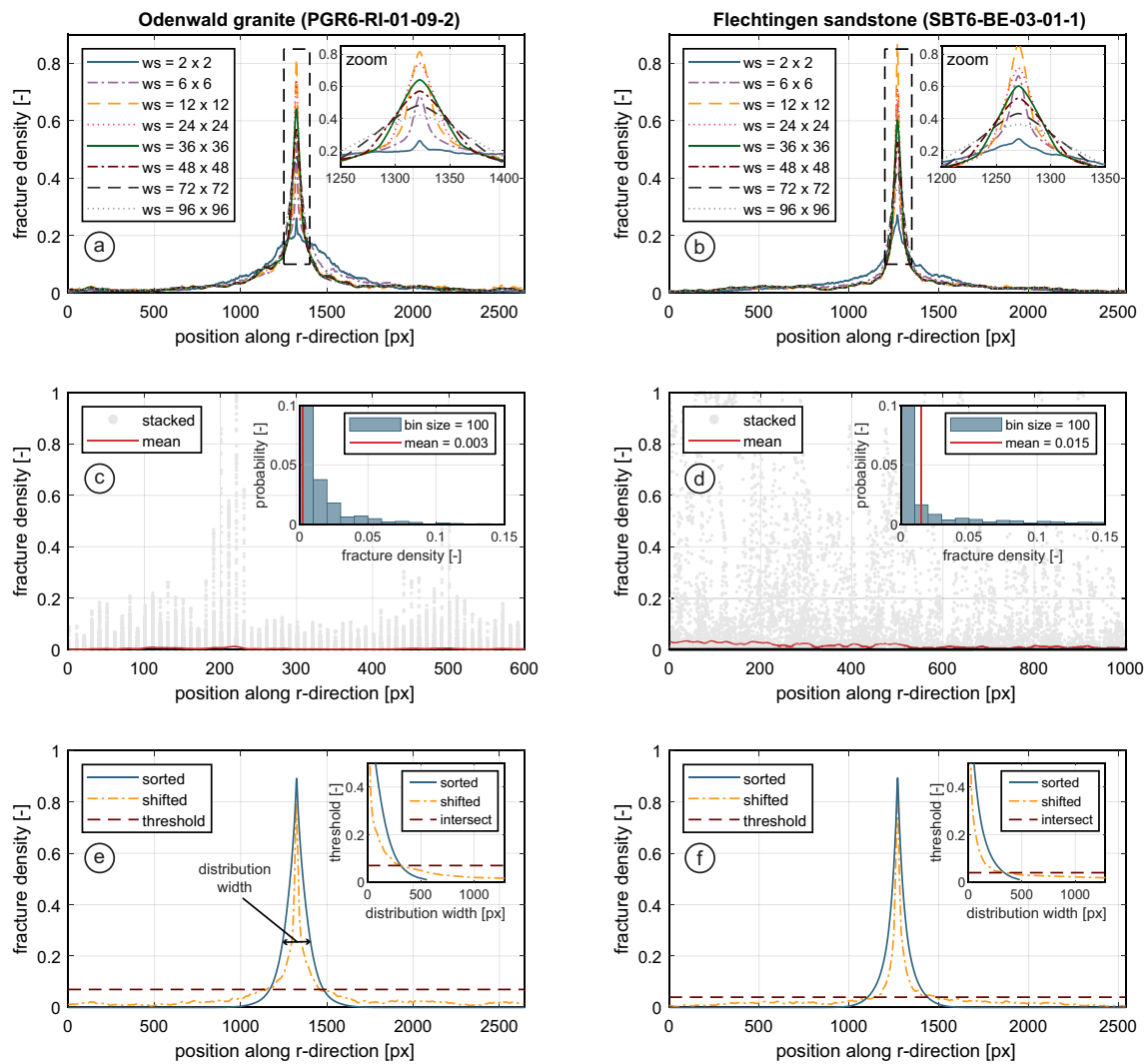


Fig. 15 Fracture density distribution: effect of window size (**a**, **b**), measured fracture density noise (**c**, **d**) and intersection of the sorted and shifted fracture density distributions (**e**, **f**)

Acknowledgements This project has received funding from the European Unions Horizon 2020 research and innovation programme under Grant agreement no. 654662, as well as the ReSalt project funded by the Federal Ministry for Economic Affairs and Energy (BMWi) under Grant agreement no. 0324244C. We would also like to thank Ronny Giese for re-designing and realizing the PTS set-up, as well as Stefan Gehrman for preparing the high quality thin sections.

Funding Open Access funding enabled and organized by Projekt DEAL.

Compliance with Ethical Standards

Conflict of Interest The authors declare that they have no conflict of interest.

Open Access This article is licensed under a Creative Commons Attribution 4.0 International License, which permits use, sharing, adaptation, distribution and reproduction in any medium or format, as long

as you give appropriate credit to the original author(s) and the source, provide a link to the Creative Commons licence, and indicate if changes were made. The images or other third party material in this article are included in the article's Creative Commons licence, unless indicated otherwise in a credit line to the material. If material is not included in the article's Creative Commons licence and your intended use is not permitted by statutory regulation or exceeds the permitted use, you will need to obtain permission directly from the copyright holder. To view a copy of this licence, visit <http://creativecommons.org/licenses/by/4.0/>.

References

- Amitrano D, Schmittbuhl J (2002) Fracture roughness and gouge distribution of a granite shear band. *J Geophys Res Solid Earth* 107(B12):ESE 19-1–ESE 19-16. <https://doi.org/10.1029/2002J B001761>

- Backers T, Stephansson O (2012) ISRM suggested method for the determination of mode II fracture toughness. *Rock Mech Rock Eng* 45(6):1011–1022. <https://doi.org/10.1007/s00603-012-0271-9>
- Barnhoorn A, Cox SF, Robinson DJ, Senden T (2010) Stress- and fluid-driven failure during fracture array growth: implications for coupled deformation and fluid flow in the crust. *Geology* 38(9):779–782. <https://doi.org/10.1130/G31010.1>
- Barton N, Bandis S, Bakhtar K (1985) Strength, deformation and conductivity coupling of rock joints. *Int J Rock Mech Min Sci Geomech Abstr* 22(3):121–140. [https://doi.org/10.1016/0148-9062\(85\)93227-9](https://doi.org/10.1016/0148-9062(85)93227-9)
- Blöcher G, Reinsch T, Hassanzadegan A, Milsch H, Zimmermann G (2014) Direct and indirect laboratory measurements of poroelastic properties of two consolidated sandstones. *Int J Rock Mech Min Sci* 67:191–201. <https://doi.org/10.1016/j.ijrmmms.2013.08.033>
- Blöcher G, Reinsch T, Hennings J, Milsch H, Regenspurg S, Kummerow J, Francke H, Kranz S, Saadat A, Zimmermann G, Huenges E (2016) Hydraulic history and current state of the deep geothermal reservoir Groß Schneck. *Geothermics* 63:27–43. <https://doi.org/10.1016/j.geothermics.2015.07.008>
- Blöcher G, Kluge C, Goense T, Pei L, Bakker RR, Bruhn D (2019) Hydraulic-mechanical characterization of geothermal reservoir rocks. In: *European geothermal congress 2019, Den Haag, The Netherlands, 11–14 June*
- Boffa JM, Allain C, Hulin J (1998) Experimental analysis of fracture rugosity in granular and compact rocks. *Eur Phys J Appl Phys* 2(3):281–289. <https://doi.org/10.1051/epjap:1998194>
- Bos B, Spiers C (2001) Experimental investigation into the microstructural and mechanical evolution of phyllosilicate-bearing fault rock under conditions favouring pressure solution. *J Struct Geol* 23(8):1187–1202. [https://doi.org/10.1016/S0191-8141\(00\)00184-X](https://doi.org/10.1016/S0191-8141(00)00184-X)
- Candela T, Renard F, Bouchon M, Brouste A, Marsan D, Schmittbuhl J, Voisin C (2009) Characterization of fault roughness at various scales: implications of three-dimensional high resolution topography measurements. *Pure Appl Geophys* 166(10–11):1817–1851. <https://doi.org/10.1007/s00024-009-0521-2>
- Candela T, Renard F, Klinger Y, Mair K, Schmittbuhl J, Brodsky EE (2012) Roughness of fault surfaces over nine decades of length scales. *J Geophys Res Solid Earth*. <https://doi.org/10.1029/2011JF009041>
- Chambon G, Schmittbuhl J, Corfdir A, Orellana N, Diraison M, Géraud Y (2006) The thickness of faults: from laboratory experiments to field scale observations. *Tectonophysics* 426(1–2):77–94. <https://doi.org/10.1016/j.tecto.2006.02.014>
- Chen L, Liu J, Wang C, Liu J, Su R, Wang J (2014) Characterization of damage evolution in granite under compressive stress condition and its effect on permeability. *Int J Rock Mech Min Sci* 71:340–349. <https://doi.org/10.1016/j.ijrmmms.2014.07.020>
- Chen Z, Narayan S, Yang Z, Rahman S (2000) An experimental investigation of hydraulic behaviour of fractures and joints in granitic rock. *Int J Rock Mech Min Sci* 37(7):1061–1071. [https://doi.org/10.1016/S1365-1609\(00\)00039-3](https://doi.org/10.1016/S1365-1609(00)00039-3)
- Cox S, Scholz C (1988) On the formation and growth of faults: an experimental study. *J Struct Geol* 10(4):413–430. [https://doi.org/10.1016/0191-8141\(88\)90019-3](https://doi.org/10.1016/0191-8141(88)90019-3)
- Darcy H (1856) *Les Fontaines Publiques de La Ville de Dijon: Exposition et Application Des Principes a Suivre et Des Formules a Employer Dans Las Questions de Distribution deau. V. Dalamont*
- Dunn DE, LaFountain LJ, Jackson RE (1973) Porosity dependence and mechanism of brittle fracture in sandstones. *J Geophys Res* 78(14):2403–2417. <https://doi.org/10.1029/JB078i014p02403>
- Elkhoury JE, Niemeijer A, Brodsky EE, Marone C (2011) Laboratory observations of permeability enhancement by fluid pressure oscillation of in situ fractured rock. *J Geophys Res*. <https://doi.org/10.1029/2010JB007759>
- Evans JP, Forster CB, Goddard JV (1997) Permeability of fault-related rocks, and implications for hydraulic structure of fault zones. *J Struct Geol* 19(11):1393–1404. [https://doi.org/10.1016/S0191-8141\(97\)00057-6](https://doi.org/10.1016/S0191-8141(97)00057-6)
- Fang Y, Elsworth D, Wang C, Ishibashi T, Fitts JP (2017) Frictional stability-permeability relationships for fractures in shales. *J Geophys Res Solid Earth* 122(3):1760–1776. <https://doi.org/10.1002/2016JB013435>
- Fang Y, Elsworth D, Wang C, Jia Y (2018) Mineralogical controls on frictional strength, stability, and shear permeability evolution of fractures. *J Geophys Res Solid Earth* 123(5):3549–3563. <https://doi.org/10.1029/2017JB015338>
- Faoro I, Niemeijer A, Marone C, Elsworth D (2009) Influence of shear and deviatoric stress on the evolution of permeability in fractured rock. *J Geophys Res Solid Earth*. <https://doi.org/10.1029/2007JB005372>
- Faulkner D, Armitage P (2013) The effect of tectonic environment on permeability development around faults and in the brittle crust. *Earth Planet Sci Lett* 375:71–77. <https://doi.org/10.1016/j.epsl.2013.05.006>
- Faulkner D, Jackson C, Lunn R, Schlichte R, Shipton Z, Wibberley C, Withjack M (2010) A review of recent developments concerning the structure, mechanics and fluid flow properties of fault zones. *J Struct Geol* 32(11):1557–1575. <https://doi.org/10.1016/j.jsg.2010.06.009>
- Fisher Q, Knipe R (2001) The permeability of faults within siliciclastic petroleum reservoirs of the North Sea and Norwegian Continental Shelf. *Mar Pet Geol* 18(10):1063–1081. [https://doi.org/10.1016/S0264-8172\(01\)00042-3](https://doi.org/10.1016/S0264-8172(01)00042-3)
- Fisher QJ, Knipe RJ (1998) Fault sealing processes in siliciclastic sediments. *Geol Soc Lond Spec Publ* 147(1):117–134. <https://doi.org/10.1144/GSL.SP.1998.147.01.08>
- Fossen H, Schultz RA, Shipton ZK, Mair K (2007) Deformation bands in sandstone: a review. *J Geol Soc* 164(4):755–769. <https://doi.org/10.1144/0016-76492006-036>
- Genter A, Cuenot N, Goerke X (2012) Status of the Soultz geothermal project during exploitation between 2010 and 2012. In: *37th Workshop on geothermal reservoir engineering, Stanford University, California, USA, Jan 2012, Stanford, United States. SGP-TR-194*
- Hansen A, Schmittbuhl J (2003) Origin of the universal roughness exponent of brittle fracture surfaces: stress-weighted percolation in the damage zone. *Phys Rev Lett*. <https://doi.org/10.1103/PhysRevLett.90.045504>
- Hassanzadegan A, Blöcher G, Milsch H, Urpi L, Zimmermann G (2014) The effects of temperature and pressure on the porosity evolution of Flechtinger sandstone. *Rock Mech Rock Eng* 47(2):421–434. <https://doi.org/10.1007/s00603-013-0401-z>
- Hofmann H, Blöcher G, Milsch H, Babadagli T, Zimmermann G (2016) Transmissivity of aligned and displaced tensile fractures in granitic rocks during cyclic loading. *Int J Rock Mech Min Sci* 87:69–84. <https://doi.org/10.1016/j.ijrmmms.2016.05.011>
- Im K, Elsworth D, Fang Y (2018) The influence of pre-slip sealing on the permeability evolution of fractures and faults. *Geophys Res Lett* 45(1):166–175. <https://doi.org/10.1002/2017GL076216>
- Ishibashi T, Fang Y, Elsworth D, Watanabe N, Asanuma H (2020) Hydromechanical properties of 3d printed fractures with controlled surface roughness: insights into shear-permeability coupling processes. *Int J Rock Mech Min Sci* 128:104271. <https://doi.org/10.1016/j.ijrmmms.2020.104271>
- Janssen C, Wagner F, Zang A, Dresen G (2001) Fracture process zone in granite: a microstructural analysis. *Int J Earth Sci* 90(1):46–59. <https://doi.org/10.1007/s005310000157>

- Kluge C, Blöcher G, Milsch H, Hofmann H, Nicolas A, Li Z, Fortin J (2017) Sustainability of fractured rock permeability under varying pressure. In: Poromechanics VI: Proceedings of the Sixth Biot Conference on Poromechanics, Paris, France. <https://doi.org/10.1061/9780784480779.148>
- Kluge C, Blöcher G, Barnhoorn A, Bruhn D (2020) Hydraulic-mechanical properties of microfaults in granitic rock using the punch-through shear test. *Int J Rock Mech Min Sci* 134:104393. <https://doi.org/10.1016/j.ijrmmms.2020.104393>
- Lockner DA, Byerlee JD, Kuksenko V, Ponomarev A, Sidorin A (1991) Quasi-static fault growth and shear fracture energy in granite. *Nature* 350(6313):39–42. <https://doi.org/10.1038/350039a0>
- Marache A, Riss J, Gentier S (2008) Experimental and modelled mechanical behaviour of a rock fracture under normal stress. *Rock Mech Rock Eng* 41(6):869–892. <https://doi.org/10.1007/s00603-008-0166-y>
- Meakin P (1998) Scaling and growth far from equilibrium. Cambridge University Press, New York
- Milsch H, Hofmann H, Blöcher G (2016) An experimental and numerical evaluation of continuous fracture permeability measurements during effective pressure cycles. *Int J Rock Mech Min Sci* 89:109–115. <https://doi.org/10.1016/j.ijrmmms.2016.09.002>
- Mitchell TM, Faulkner DR (2008) Experimental measurements of permeability evolution during triaxial compression of initially intact crystalline rocks and implications for fluid flow in fault zones. *J Geophys Res*. <https://doi.org/10.1029/2008JB005588>
- Moore D, Lockner D (1995) The role of microcracking in shear-fracture propagation in granite. *J Struct Geol* 17(1):95–114. [https://doi.org/10.1016/0191-8141\(94\)E0018-T](https://doi.org/10.1016/0191-8141(94)E0018-T)
- Myers R, Aydin A (2004) The evolution of faults formed by shearing across joint zones in sandstone. *J Struct Geol* 26(5):947–966. <https://doi.org/10.1016/j.jsg.2003.07.008>
- Nicolas A, Blöcher G, Kluge C, Li Z, Hofmann H, Pei L, Milsch H, Fortin J, Guéguen Y (2020) Pore pressure pulse migration in microcracked andesite recorded with fibre optic sensors. *Geomech Energy Environ* 24:100183. <https://doi.org/10.1016/j.gete.2020.100183>
- Niemeijer AR, Spiers CJ (2005) Influence of phyllosilicates on fault strength in the brittle-ductile transition: insights from rock analogue experiments. *Geol Soc Lond Spec Publ* 245(1):303–327. <https://doi.org/10.1144/GSL.SP.2005.245.01.15>
- Orywall P, Drüppel K, Kuhn D, Kohl T, Zimmermann M, Eiche E (2017) Flow-through experiments on the interaction of sandstone with ba-rich fluids at geothermal conditions. *Geotherm Energy*. <https://doi.org/10.1186/s40517-017-0079-7>
- Passelègue FX, Brantut N, Mitchell TM (2018) Fault reactivation by fluid injection: controls from stress state and injection rate. *Geophys Res Lett*. <https://doi.org/10.1029/2018GL080470>
- Pei L, Blöcher G, Milsch H, Deon F, Zimmermann G, Rühaak W, Sass I, Huenges E (2016) Thermal strain in a water-saturated limestone under hydrostatic and deviatoric stress states. *Tectonophysics* 688:49–64. <https://doi.org/10.1016/j.tecto.2016.09.020>
- Pollard DD (2005) Fundamentals of structural geology. Cambridge University Press, Cambridge
- Pyrak-Nolte L, Morris J (2000) Single fractures under normal stress: the relation between fracture specific stiffness and fluid flow. *Int J Rock Mech Min Sci* 37(1–2):245–262. [https://doi.org/10.1016/S1365-1609\(99\)00104-5](https://doi.org/10.1016/S1365-1609(99)00104-5)
- Reches Z, Lockner DA (1994) Nucleation and growth of faults in brittle rocks. *J Geophys Res Solid Earth* 99(B9):18159–18173. <https://doi.org/10.1029/94JB00115>
- Santucci S, Grob M, Toussaint R, Schmittbuhl J, Hansen A, Maløy KJ (2010) Fracture roughness scaling: a case study on planar cracks. *EPL (Europhys Lett)* 92(4):44001. <https://doi.org/10.1209/0295-5075/92/44001>
- Schmittbuhl J, Schmitt F, Scholz C (1995a) Scaling invariance of crack surfaces. *J Geophys Res Solid Earth* 100(B4):5953–5973. <https://doi.org/10.1029/94JB02885>
- Schmittbuhl J, Vilotte JP, Roux S (1995b) Reliability of self-affine measurements. *Phys Rev E* 51(1):131–147. <https://doi.org/10.1103/PhysRevE.51.131>
- Schneider C, Rasband W, Eliceiri K (2012) NIH image to ImageJ: 25 years of image analysis. *Nat Methods* 9(7):671–675. <https://doi.org/10.1038/nmeth.2089>
- Segall P, Pollard DD (1983) Nucleation and growth of strike slip faults in granite. *J Geophys Res* 88(B1):555. <https://doi.org/10.1029/JB088iB01p00555>
- Stünitz H, Keulen N, Hirose T, Heilbronner R (2010) Grain size distribution and microstructures of experimentally sheared granitoid gouge at coseismic slip rates—criteria to distinguish seismic and aseismic faults? *J Struct Geol* 32(1):59–69. <https://doi.org/10.1016/j.jsg.2009.08.002>
- Tenthorey E, Cox SF (2006) Cohesive strengthening of fault zones during the interseismic period: an experimental study. *J Geophys Res*. <https://doi.org/10.1029/2005JB004122>
- Terzaghi K (1925) *Erdbaumechanik Auf Bodenphysikalischer Grundlage*. Leipzig u. Wien, F. Deuticke
- Teufel LW (1987) Permeability changes during shear deformation of fractured rock. In: 28. US symposium on rock mechanics, Tucson, AZ, USA, 29 June
- Vermilye JM, Scholz CH (1999) Fault propagation and segmentation: insight from the microstructural examination of a small fault. *J Struct Geol* 21(11):1623–1636. [https://doi.org/10.1016/S0191-8141\(99\)00093-0](https://doi.org/10.1016/S0191-8141(99)00093-0)
- Watanabe N, Hirano N, Tsuchiya N (2009) Diversity of channeling flow in heterogeneous aperture distribution inferred from integrated experimental-numerical analysis on flow through shear fracture in granite. *J Geophys Res*. <https://doi.org/10.1029/2008JB005959>
- Wibberley CA, Petit JP, Rives T (2000) Micromechanics of shear rupture and the control of normal stress. *J Struct Geol* 22(4):411–427. [https://doi.org/10.1016/S0191-8141\(99\)00158-3](https://doi.org/10.1016/S0191-8141(99)00158-3)
- Wong TF (1982) Micromechanics of faulting in westerly granite. *Int J Rock Mech Min Sci Geomech Abstr* 19(2):49–64. [https://doi.org/10.1016/0148-9062\(82\)91631-X](https://doi.org/10.1016/0148-9062(82)91631-X)
- Yasuhara H, Elsworth D (2008) Compaction of a rock fracture moderated by competing roles of stress corrosion and pressure solution. *Pure Appl Geophys* 165(7):1289–1306. <https://doi.org/10.1007/s00024-008-0356-2>
- Ye Z, Ghassemi A (2019) Injection-induced propagation and coalescence of preexisting fractures in granite under triaxial stress. *J Geophys Res Solid Earth* 124(8):7806–7821. <https://doi.org/10.1029/2019JB017400>
- Zang A, Wagner FC, Stanchits S, Janssen C, Dresen G (2000) Fracture process zone in granite. *J Geophys Res Solid Earth* 105(B10):23651–23661. <https://doi.org/10.1029/2000JB900239>
- Zhang Q, Li X, Bai B, Pei L, Shi L, Wang Y (2019) Development of a direct-shear apparatus coupling with high pore pressure and elevated temperatures. *Rock Mech Rock Eng* 52(9):3475–3484. <https://doi.org/10.1007/s00603-019-1735-y>
- Zoback MD, Byerlee JD (1975) The effect of microcrack dilatancy on the permeability of westerly granite. *J Geophys Res* 80(5):752–755. <https://doi.org/10.1029/jb080i005p00752>

Publisher's Note Springer Nature remains neutral with regard to jurisdictional claims in published maps and institutional affiliations.